Article

Cell Host & Microbe

UBE2O-mediated monoubiquitination licenses NLRP6 inflammasome activation in the intestine

Graphical abstract

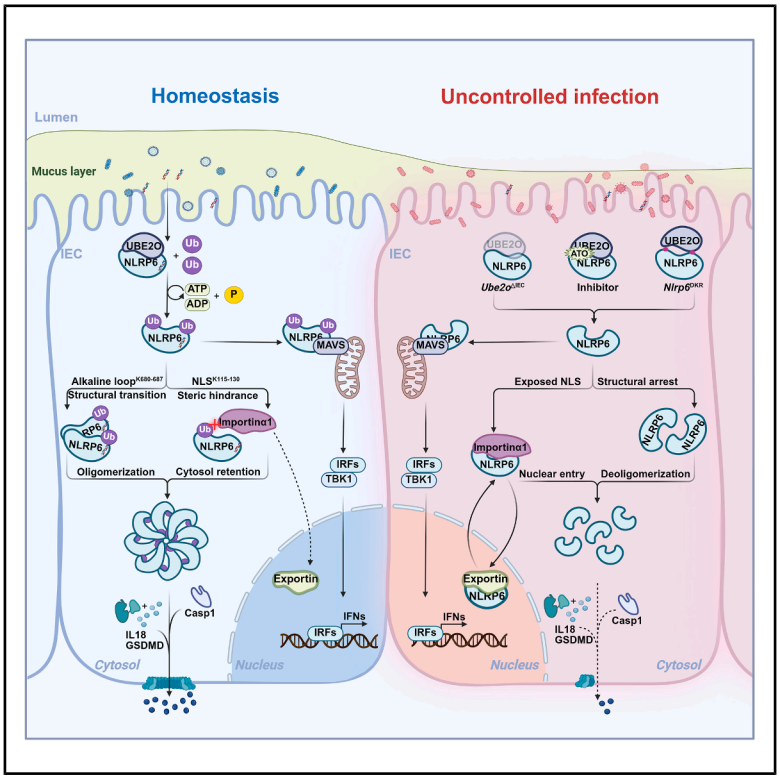

Highlights

- UBE2O mediates NLRP6 monoubiquitination in IECs in response to microbial signals
- UBE2O-mediated NLRP6 monoubiquitination determines inflammasome activation
- Monoubiquitination coordinately activates NLRP6 through dual site-specific mechanisms
- Disruption of the UBE2O-NLRP6 axis exacerbates intestinal pathogen infection

Authors

Decai Wang, Xuequn Chen, Kaiwen Sui, ..., Kankan Wang, Jie Zheng, Shu Zhu

Correspondence

zhushu@ustc.edu.cn

In brief

Wang et al. demonstrate that UBE2O-mediated monoubiquitination is a dual-purpose switch for NLRP6 activation. Site-specific monoubiquitination at K680–687 and K115–130 coordinately promotes inflammasome assembly by inducing conformational changes that promote oligomerization and ensures cytoplasmic localization by imposing a steric blockade on importin, respectively.

Wang et al., 2026, Cell Host & Microbe *34*, 86–102
January 14, 2026 © 2025 Elsevier Inc. All rights are reserved, including those for text and data mining, AI training, and similar technologies.
https://doi.org/10.1016/j.chom.2025.12.009

CellPress

CellPress

Cell Host & Microbe

Article

UBE2O-mediated monoubiquitination licenses NLRP6 inflammasome activation in the intestine

Decai Wang,[1,10] Xuequn Chen,[1,10] Kaiwen Sui,[1] Anlei Wang,[1] Runzhi Li,[1] Weijun Zhou,[2] Xiaoyu Zhu,[3] Yan Hua,[4] Shuanghu Yuan,[5] Rongbin Zhou,[1] Fangyi Dong,[6] Kankan Wang,[7] Jie Zheng,[8] and Shu Zhu[1,9,11,*]

[1]State Key Laboratory of Immune Response and Immunotherapy, Center for Advanced Interdisciplinary Science and Biomedicine of IHM, Division of Life Sciences and Medicine, University of Science and Technology of China, Hefei 230026, China
[2]Department of Hematology, Zhujiang Hospital, Southern Medical University, Guangzhou 510282, China
[3]Department of Hematology, The First Affiliated Hospital of University of Science and Technology of China, Division of Life Sciences and Medicine, University of Science and Technology of China, Hefei 230001, China
[4]Department of Laboratory Medicine, The First Affiliated Hospital of University of Science and Technology of China, Division of Life Sciences and Medicine, University of Science and Technology of China, Hefei 230001, China
[5]Department of Radiation Oncology, The First Affiliated Hospital of University of Science and Technology of China, Division of Life Sciences and Medicine, University of Science and Technology of China, Hefei 230001, China
[6]Department of Hematology, State Key Laboratory of Medical Genomics, Ruijin Hospital Affiliated to Shanghai Jiao Tong University School of Medicine, Shanghai 200025, China
[7]Shanghai Institute of Hematology, State Key Laboratory of Medical Genomics, National Research Center for Translational Medicine at Shanghai, Ruijin Hospital Affiliated to Shanghai Jiao Tong University School of Medicine, Shanghai 200025, China
[8]Shanghai Institute of Virology, Shanghai Jiao Tong University School of Medicine, Shanghai 200025, China
[9]Department of Digestive Disease, The First Affiliated Hospital of University of Science and Technology of China, Division of Life Sciences and Medicine, University of Science and Technology of China, Hefei 230001, China
[10]These authors contributed equally
[11]Lead contact
*Correspondence: zhushu@ustc.edu.cn
https://doi.org/10.1016/j.chom.2025.12.009

SUMMARY

The NLRP6 inflammasome in intestinal epithelial cells (IECs) is a key sentinel of enteric pathogens, yet its activation mechanism remains enigmatic. Here, we identify monoubiquitination as a critical post-translational switch for NLRP6 inflammasome activation. We demonstrate that the E3 ligase UBE2O catalyzes dual-site monoubiquitination of NLRP6: at K680-687 to drive oligomerization via a conformational change, and at K115/130 within the nuclear localization signal to enforce cytoplasmic sequestration through steric hindrance. Mice harboring UBE2O deficiency or monoubiquitination-resistant NLRP6 mutations exhibit defective inflammasome activation and heightened susceptibility to rotavirus and *Citrobacter rodentium* infection. Furthermore, the UBE2O inhibitor arsenic trioxide suppresses NLRP6-dependent interleukin (IL)-18 secretion in acute promyelocytic leukemia (APL) patients. Thus, UBE2O-mediated dual-site monoubiquitination emerges as a central mechanism licensing NLRP6 inflammasome activation, revealing a new target for modulating intestinal immunity.

INTRODUCTION

The innate immune system functions as the first line of host defense against pathogens, relying on pattern recognition receptors (PRRs) that respond to pathogen-associated molecular patterns (PAMPs) and danger-associated molecular patterns (DAMPs) to trigger inflammatory responses and programmed cell death.[1] NLRP6, an intestinal epithelial cells (IECs)-specific NLR family member, operates within a complex and dynamic environment (e.g., rich commensals and occasional infections) in the intestine by initiating the inflammasome pathway and the type I interferon (IFN) pathway to maintain intestinal homeostasis.[2–9] However, the molecular mechanism by which the host distinguishes between the NLRP6-mediated inflammasome pathway and the NLRP6-mediated IFN pathway remains completely unknown, and the molecular mechanism underlying NLRP6 inflammasome activation remains largely unknown.

The canonical PRRs expressed in immune cells, such as Toll-like receptor (TLR)4, cGAS, RIG-I, Dectin-1, ZBP1, and NLRP3, have been reported to utilize multiple post-translational modifications (PTMs) to control the "initiation," "amplification," and "termination" of immune responses to the environmental stimuli.[10–18] NLRP6 has only been reported to undergo K63-linked deubiquitination by the "eraser" CYLD, thereby enhancing the interaction between ASC and NLRP6 to activate inflammasome signaling.[8] However, the molecular details of

All rights are reserved, including those for text and data mining, AI training, and similar technologies.

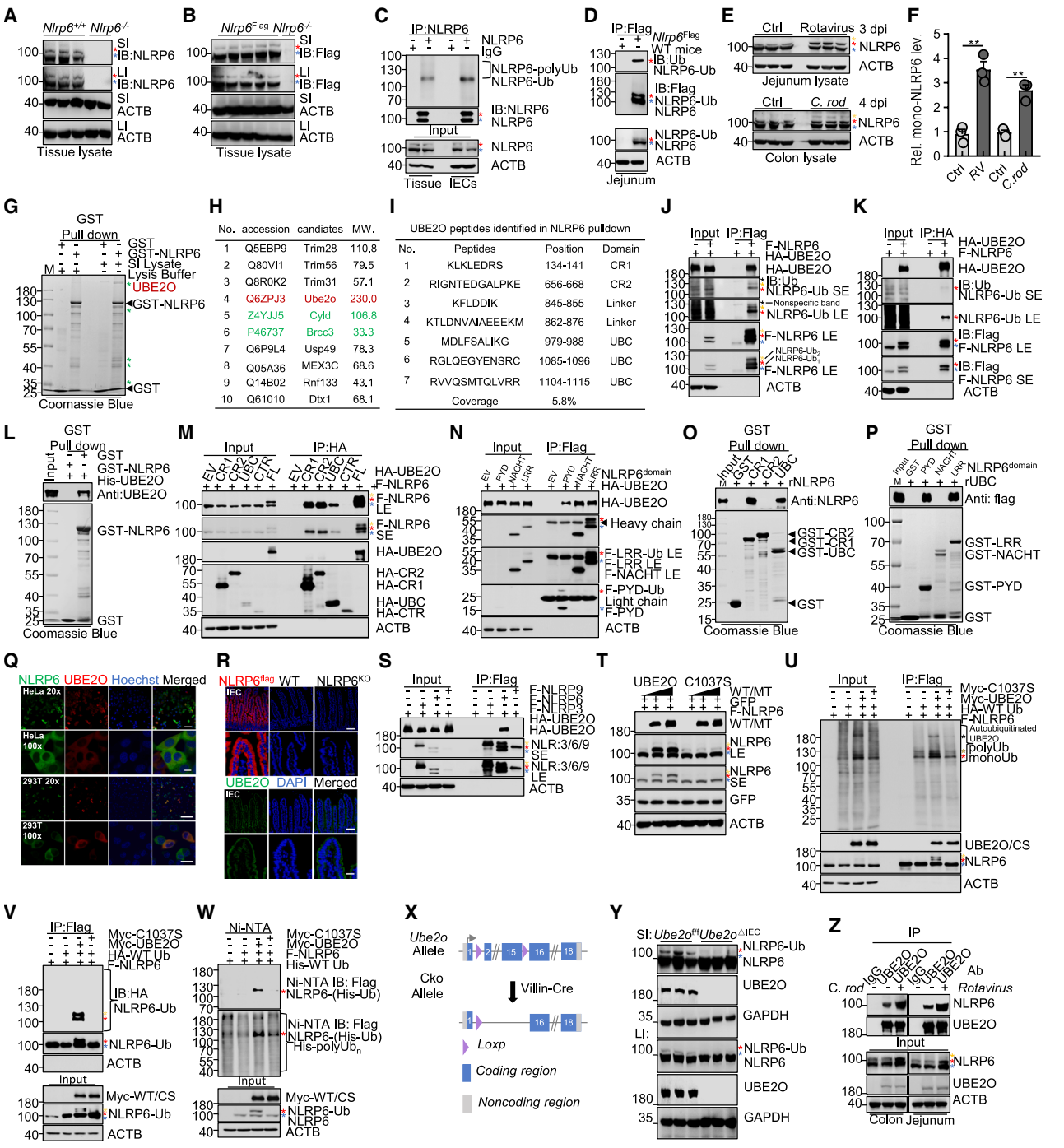

Figure 1. UBE2O mediates NLRP6 monoubiquitination in IECs in response to microbial signals

(A and B) Western blotting of NLRP6 in intestinal tissues from indicated mice.

(C) IP of NLRP6 in WT mice, followed by western blotting.

(D) IP of NLRP6 in *Nlrp6*$^{FLAG/FLAG}$ mice, followed by western blotting.

(E) Western blotting of NLRP6 in jejunum (RV) or colon (*C. rodentium*) post infection.

(F) Statistics of NLRP6 monoubiquitination in (E).

(G) Coomassie blue staining of NLRP6 and NLRP6-binding proteins (green asterisks).

(H) Top 10 UME candidates identified by LC-MS/MS. Proteins with sizes matching the most obvious interacting band (>180 kDa) are labeled in red.

(I) UBE2O peptides identified by LC-MS/MS.

(J and K) Reciprocal co-IP between NLRP6 and UBE2O in HEK293T cells.

(L) *In vitro* binding assay with purified His-UBE2O and GST-NLRP6.

(legend continued on next page)

how a specific modification drives NLRP6 activation, which "writer" drives NLRP6 modification, and the physiological consequences of depleting either the modification or the writer remain completely unexplored.

Unlike polyubiquitination, which has largely been associated with protein signaling or degradation through sequential ubiquitin linkage by approximately 700 ubiquitin (Ub)-modifying enzymes (UMEs),[19,20] monoubiquitination has been widely linked to chromatin regulation, protein sorting, assembly, and trafficking through covalent conjugation to a lysine residue of substrates by approximately 20 reported enzymes.[21] UBE2O is an E2/E3 hybrid enzyme with atypical E3 ligase activity, and previous studies have mainly reported its functions in cancer.[22–26] It has been reported to polyubiquitinate K470 of AMPKα2 to inhibit tumor progression through the mTOR-HIF1α pathway,[26] and monoubiquitinate the NLS of BAP1 to regulate cell cycle and differentiation by maintaining cytoplasmic sequestration.[25] However, the physiological substrate and function of UBE2O in the intestine, the involvement of monoubiquitination in the activation of the NLR family, and the molecular insights into how monoubiquitination distinguishes and determines NLRP6-mediated signaling are completely unknown.

Here, we detected robust monoubiquitination, but not polyubiquitination, of NLRP6 in IECs in response to microbial signals. We found that UBE2O monoubiquitinates NLRP6 at K680–687 to facilitate oligomerization and at K115–130 within an NLS region of NLRP6 to mediate cytoplasmic sequestration. Mice with UBE2O deletion (*Ube2o*$^{\Delta IEC}$) or NLRP6 mutation (*Nlrp6*^{DKR}) in IECs exhibit impaired NLRP6 inflammasome activation and defense against *Citrobacter rodentium* and rotavirus (RV) infection. Together, our findings demonstrate a model of inflammasome activation driven by NLR monoubiquitination, and provide insights into the molecular mechanisms underlying NLRP6 inflammasome activation.

RESULTS

NLRP6 is monoubiquitinated in IECs in response to microbial signals

Mass spectrometry (MS) analysis revealed that ubiquitination and phosphorylation signals are readily detectable on NLRP6 in IECs from *Nlrp6*$^{FLAG/FLAG}$ mice (Figures S1A and S1B). Further validation in cells overexpressing FLAG-tagged NLRP6 indicated that an upper band of NLRP6 was detected by anti-NLRP6 or anti-FLAG antibody (Figure S1C). Based on the molecular size (>5 kDa), this modification is more likely monoubiquitination (~8 kDa) rather than phosphorylation (<3 kDa). Indeed, we detected this upper band using an anti-Ub antibody rather than other PTM antibodies (Figure S1C). Importantly, we detected the upper band (~105 kDa) in both intestinal tissues and IECs using either anti-NLRP6 or anti-FLAG antibody (Figures 1A, 1B, and S1D). We further confirmed that monoubiquitinated NLRP6 can be detected by anti-Ub antibody following immunoprecipitation with anti-NLRP6 or anti-FLAG antibody (Figures 1C and 1D). Notably, the NLRP6 upper band increased during pathogen infection in the intestine, and an additional upper band was observed during infection, although weaker than the previously identified one (Figures 1E, 1F, and S1E–S1G). These data suggest that the inducible monoubiquitination(s) on NLRP6 may play a role in antimicrobial defense.[4,7,9]

UBE2O mediates NLRP6 monoubiquitination *in vitro* and *in vivo*

To identify potential UMEs for NLRP6 monoubiquitination, we performed pull-down/MS by incubating NLRP6 with IEC lysate (Figure S1H). Several known NLRP6-binding proteins were detected, including ASC, CYLD, and BRCC3 (Figures 1G, 1H, S1I, and S1J).[3,8,27] UBE2O, a 230 kDa E3 ligase,[23,24] was identified and validated to directly bind to and modify NLRP6 (Figures 1I–1L and S1K–S1O). Moreover, the results indicated that NLRP6 interacts with the conserved region 1 (CR1), conserved region 2 (CR2), and ubiquitin-conjugating (UBC) domains in cells (Figures 1M and S1P). UBE2O interacts with all three domains of NLRP6 and induces modification in both pyrin domain (PYD) and leucine-rich repeat (LRR) domains (Figures 1N, S1Q, and S1R), which is consistent with the findings of two modified bands during infection (Figure 1E). An *in vitro* binding assay indicated that UBE2O binds directly to the PYD and LRR domains, and that NLRP6 binds directly to the CR1 and UBC domains (Figures 1O, 1P, S1S, and S1T). Single-cell RNA (scRNA) sequencing data[28] showed that NLRP6 and UBE2O are co-expressed in IECs, although UBE2O is also expressed in immune cells (Figure S1U). Live-cell imaging in cells and immunofluorescence in tissues showed that NLRP6 and UBE2O co-localize in the cytoplasm (Figures 1Q, 1R, and S1V). Furthermore, we found that UBE2O only binds to and modifies

(M and N) Reciprocal co-IP between NLRP6 and UBE2O truncations in cells.
(O and P) Reciprocal co-IP between NLRP6 and UBE2O truncations *in vitro*.
(Q) Representative images of stably transfected UBE2O and NLRP6 in cells. Scale bars, 50 or 10 μm.
(R) Representative images with anti-FLAG or anti-UBE2O antibody in proximal small intestine sections. Scale bars, 50 or 20 μm.
(S) Co-IP of UBE2O with intestinal NLRs.
(T) Western blotting of NLRP6 co-expressed with UBE2O WT/C1037S.
(U) Ubiquitination assay by pull-down NLRP6 in HEK293T cells transfected with the indicated plasmids.
(V) Ubiquitination assay by pull-down NLRP6 with Ub K0 in HEK293T cells.
(W) Ubiquitination assay by pull-down Ub in HEK293T cells transfected with the indicated plasmids.
(X) Illustration of the CRISPR-Cas9 strategy used to generate *Ube2o*$^{\Delta IEC}$ mice.
(Y) Western blotting of NLRP6 in small intestine and colon tissues.
(Z) Endogenous co-IP between NLRP6 and UBE2O post infection.
Data in (A)–(E), (I)–(W), (Y), and (Z) represent ≥3 experiments. Blue, red, and yellow asterisks indicate unmodified, single-monoubiquitinated, and multi-monoubiquitinated NLRP6, respectively. Data in (F) are shown as mean ± SEM. Two-group comparisons were performed using Student's *t* tests (ns, $^{*}p < 0.05$, $^{**}p < 0.01$, $^{***}p < 0.001$, $^{**}p < 0.0001$).
See also Figure S1.

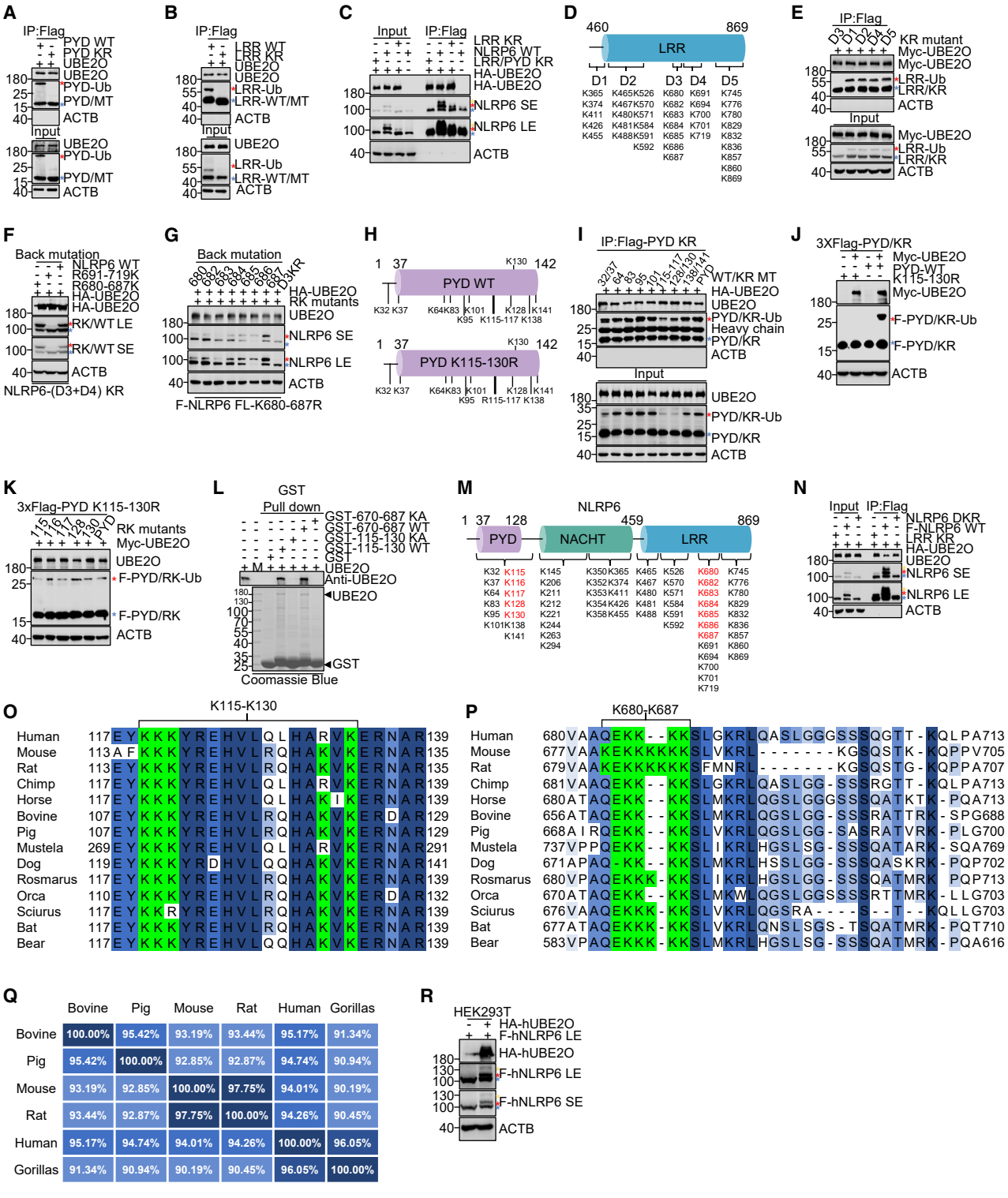

Figure 2. UBE2O mediates NLRP6 monoubiquitination at conserved K115–130 and K680–687 residues

(A) Monoubiquitination of PYD and K-to-R mutant.

(B) Monoubiquitination of LRR and K-to-R mutant.

(C) Co-IP of UBE2O with modified or unmodified NLRP6 mutants.

(D) Schematic representation of LRR domain mutants.

(E) Mapping of the modified region on LRR domain.

(F) Western blotting of monoubiquitination on NLRP6$^{K680–719R}$ with back mutation.

(legend continued on next page)

NLRP6, but not NLRP3 or NLRP9, in an enzyme activity-dependent manner (Figures 1S, 1T, S1W, and S1X). NLRP6 monoubiquitination was blocked in cells treated with AsIII (ATO [arsenic trioxide] in solution), a UBE2O inhibitor and also a first-line drug for acute promyelocytic leukemia (APL) (Figures S1Y–S1A′; Table S3). Further ubiquitination assays showed covalent conjugation between NLRP6 and Ub in the existence of UBE2O (Figures 1U–1W).

To examine the effect of UBE2O on NLRP6 *in vivo*, we generated mice with IEC-specific depletion of UBE2O (*Ube2o*$^{\Delta IEC}$) mice. We found that UBE2O is required for NLRP6 monoubiquitination *in vivo* without altering its expression (Figures 1X, 1Y, and S1B′–S1E′; Table S3). Pharmacological blockade of UBE2O also inhibited NLRP6 monoubiquitination *in vivo* (Figure S1F′). Moreover, microbial infections *in vivo* facilitated the interaction between UBE2O and NLRP6, which led to increased NLRP6 monoubiquitination (Figures 1Z, S1G′, and S1H′; Table S3). Together, the data above suggest that UBE2O is the first writer of NLRP6 and mediates its monoubiquitination in response to microbial signals.

UBE2O mediates NLRP6 monoubiquitination at K115–130 and K680–687

We found that UBE2O mainly targets canonical lysine residues because KR mutations (replacing lysine with arginine residues) in either full-length NLRP6 or the PYD/LRR domains blocked the modifications (Figures 2A–2C and S2A–S2D; Table S2). A total of 63 single KR mutations or multiple KR mutations (when lysines were proximal) in NLRP6 had no effect on the UBE2O-induced modification (Figure S2E; Table S2), suggesting that UBE2O may randomly select a single lysine within a specific region that is enriched with lysine residues. We then generated a series of NLRP6 mutants with multiple KR mutations in either the LRR or PYD. The D3 mutant (K680–687R) completely blocked UBE2O-induced LRR modification (Figures 2D, 2E, S2F, and S2G; Table S2), and back-mutations of all seven arginine residues to lysine restored the modification (Figures 2F and S2H; Table S2). Back mutation with a single lysine indicated that any one of the seven lysine residues of K680–687 restored the LRR modification (Figure 2G; Table S2), whereas mutation of any six out seven lysine residues to arginine did not affect the LRR modification (Figure S2I; Table S2), suggesting UBE2O induces LRR monoubiquitination on a random lysine residue within K680–K687 region. Similarly, UBE2O-induced PYD modification was markedly inhibited by replacing lysines 115–117 or lysines 128 and 130 with arginine, and was completely blocked by K115–130R mutation (Figures 2H–2J; Table S2). In addition, UBE2O can modify any of the five lysine residues within K115–130 (Figures 2K and 2H; Table S2), suggesting that UBE2O induces monoubiquitination on a random lysine residue within the K115–K130 region.

Both the PYD and LRR regions in NLRP6 directly interacted with UBE2O *in vitro* (Figure 2L). The NLRP6 K115–130R/K680–687R mutation (NLRP6^{DKR}) completely blocked UBE2O-induced monoubiquitination (Figures 2M, 2N, and S2J; Table S2). Lysines in K115–130 and K680–687 are located in open regions of NLRP6 predicted by AlphaFold (Figures S2K–S2M), and both regions showed interaction with the catalytic domain of UBE2O in a predicted complex[29] (Figures S2N and S2O). Lysines in K115–130 and K680–687, as well as the UBE2O, are highly conserved across species (Figures 2O–2Q). Human UBE2O also monoubiquitinates human NLRP6 (Figure 2R). These data suggest a highly conserved UBE2O-NLRP6 axis in IECs.

Monoubiquitination determines NLRP6 inflammasome activation *in vitro*

NLRP6 regulates both inflammasome and IFN pathways.[6,9] Neither UBE2O overexpression nor knockdown altered NLRP6 degradation (Figures S3A–S3F). Strikingly, UBE2O facilitated NLRP6 inflammasome activation in both an enzyme activity-dependent and monoubiquitination-dependent manner in the inflammasome reconstruction system, as evidenced by detectable active p20 and GSDMD-N_{30}, whereas NLRP6 monoubiquitination was dispensable for the IFN pathway, as evidenced by preserved binding capacity between NLRP6 and DHX15 (Figures 3A–3C and S3G–S3L). Pharmacological inhibition of UBE2O with AsIII also suppressed NLRP6 inflammasome activation (Figure 3D). Either K115–130R mutation or the K680–687R mutation inhibited NLRP6 inflammasome activation (Figures 3E and 3F), indicating that monoubiquitination at both regions is important for inflammasome pathway. Consistently, we observed impaired ASC oligomerization initiated by the NLRP6^{DKR} mutant (Figure 3G). In cellular systems, transient overexpression of NLRP6 with ASC potently induces a filamentous ASC network rather than ASC foci in BMDMs, and NLRP6 exhibits complete co-localization with ASC filaments, suggesting that the NLRP6 inflammasome is hyperactivated in cells[30,31] (Figures S3M–S3S). Further ASC filament formation and lactate dehydrogenase (LDH) release assay showed that wild-type (WT) NLRP6, but not NLRP6^{DKR}, effectively colocalized with

(G) Monoubiquitination of NLRP6$^{K680–687R}$ and the indicated mutants.
(H) Schematic representation of NLRP6 with KR mutations in PYD.
(I) Mapping of NLRP6 monoubiquitination site(s) in PYD.
(J) Western blotting of monoubiquitination on PYD^{WT} and PYD$^{K115–130R}$.
(K) Western blotting of monoubiquitination on PYD and back mutants.
(L) *In vitro* binding assay with purified protein or peptides.
(M) Schematic representation of UBE2O-targeted NLRP6 lysine residues.
(N) Western blotting of monoubiquitination on NLRP6$^{K115–130R\ plus\ K680–687R}$.
(O and P) Evolutionary conservation of K115–K130 and K680–K687.
(Q) Evolutionary conservation of UBE2O as a percent identity matrix.
(R) Monoubiquitination of human NLRP6 by human UBE2O.
Data in (A)–(C), (E)–(G), (I)–(K), (N), and (R) represent ≥3 experiments. Blue, red, and yellow asterisks indicate unmodified, single-monoubiquitinated, and multi-monoubiquitinated NLRP6, respectively.
See also Figure S2 and Table S2.

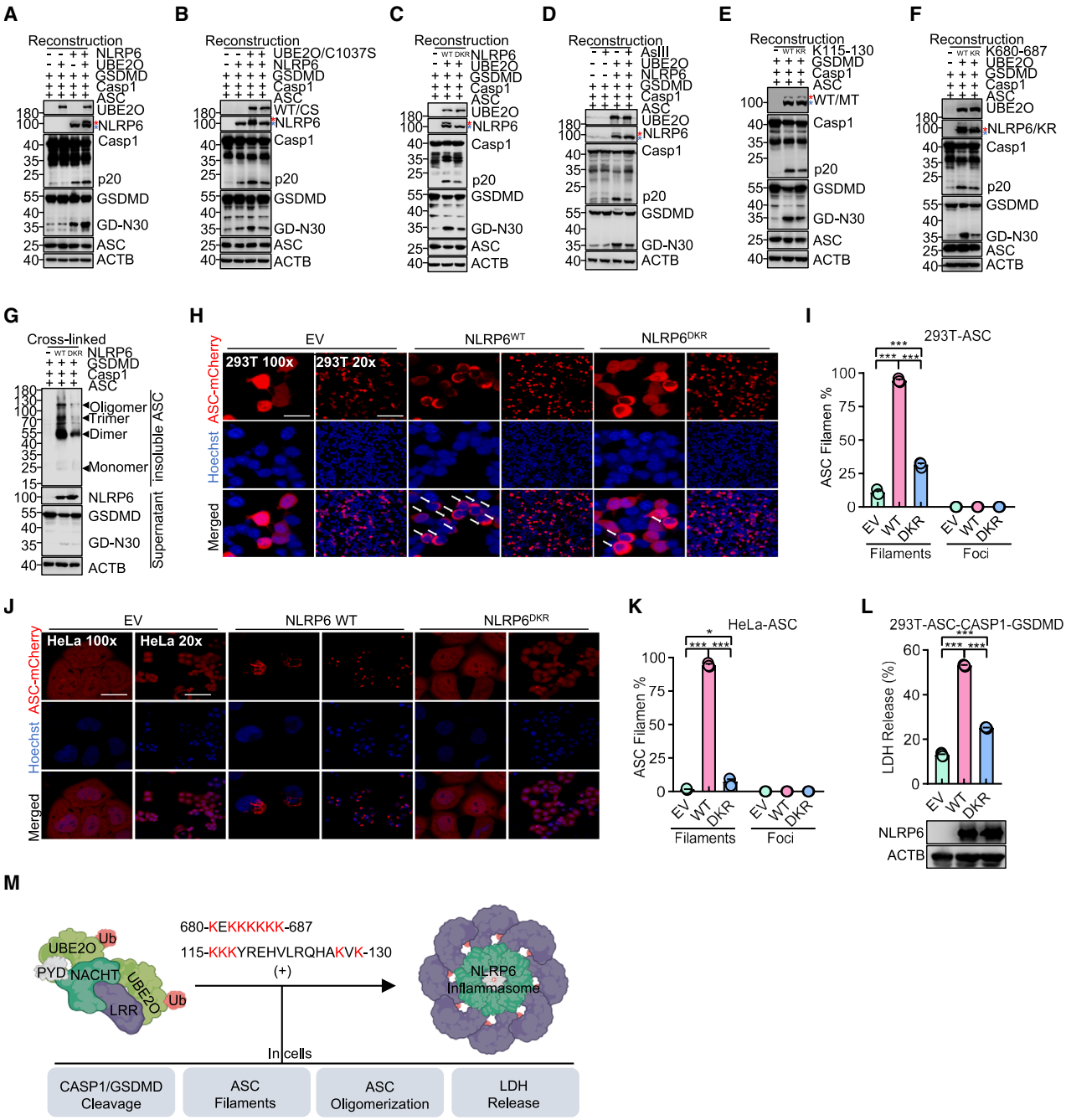

Figure 3. Monoubiquitination determines NLRP6 inflammasome activation *in vitro*

(A–C) NLRP6 inflammasome activation in cells co-expressed with indicated plasmids.

(D) NLRP6 inflammasome activation in cells co-expressed with indicated plasmids treated with AsIII.

(E) Inflammasome activation in cells co-expressed with $NLRP6^{WT}$ and $NLRP6^{K115–130R}$.

(F) Inflammasome activation in cells co-expressed with $NLRP6^{WT}$ or $NLRP6^{K680–687R}$.

(G) ASC oligomerization in inflammasome reconstruction co-expressing the indicated plasmids.

(H–K) Representative confocal imaging of ASC filaments in HEK293T (H) or HeLa (J) cells co-expressing the indicated plasmids, and quantifications of cells with ASC filaments in HEK293T (I) and HeLa (K).

(L) LDH levels of the supernatant of HEK293T cells co-expressing the indicated plasmids.

(M) Evidence of monoubiquitination-driven NLRP6 inflammasome activation in cells.

Data in (A)–(L) represent ≥3 experiments. Blue, red, and yellow asterisks indicate unmodified, single-monoubiquitinated, and multi-monoubiquitinated NLRP6, respectively. Data in (I), (K), and (L) are shown as mean ± SEM. Two-group comparisons were performed using Student's *t* tests; comparisons of more than two groups were performed using ANOVA (ns, $*p < 0.05$, $**p < 0.01$, $***p < 0.001$, $**p < 0.0001$).

See also Figure S3.

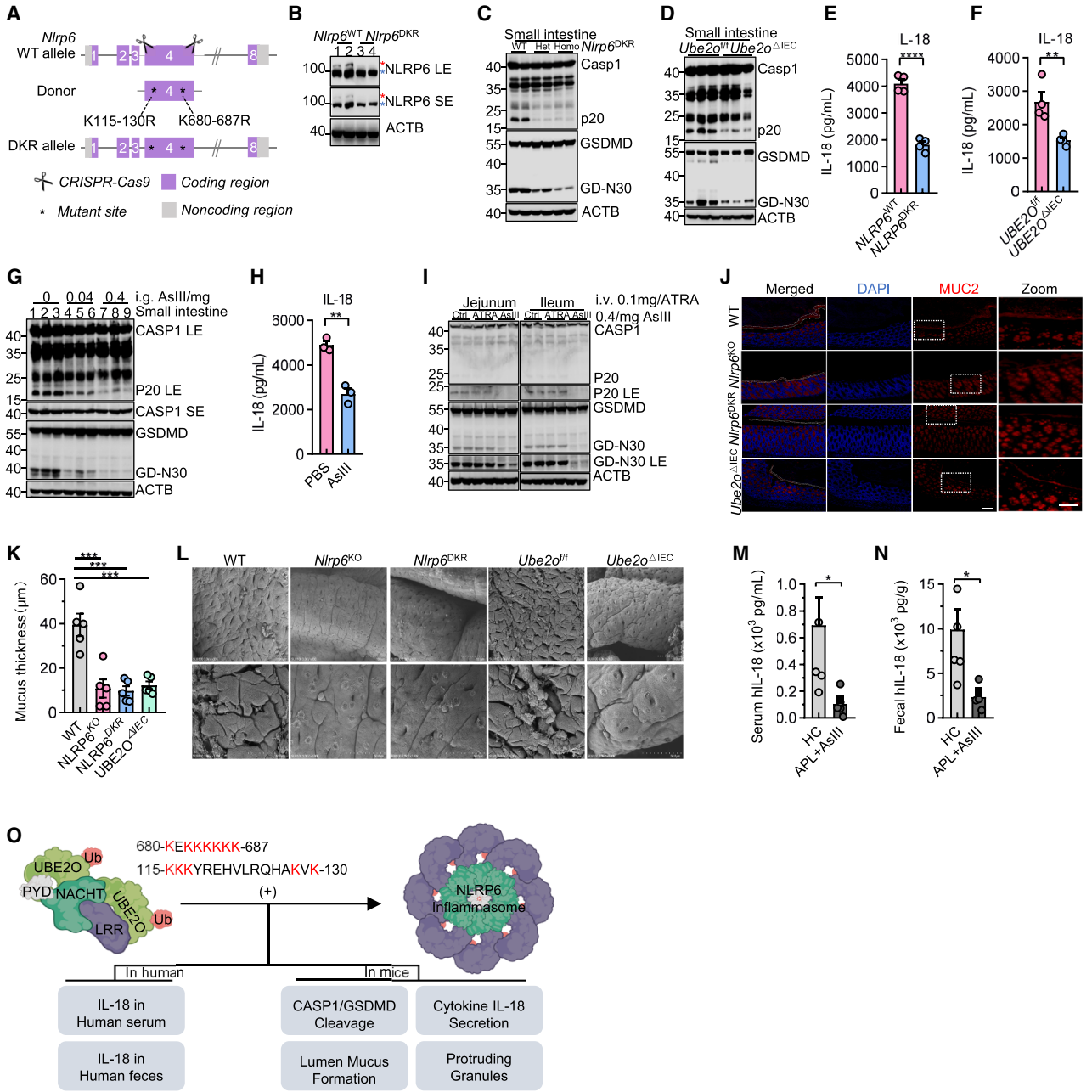

Figure 4. Monoubiquitination determines NLRP6 inflammasome activation *in vivo*

(A) Illustration of the CRISPR-Cas9 strategy used to generate *Nlrp6*^{DKR} mice.
(B) Western blotting of NLRP6 monoubiquitination in tissues from the indicated mice.
(C) Intestinal inflammasome activation in *Nlrp6*$^{HET\ DKR}$, *Nlrp6*^{DKR}, and littermate WT mice.
(D) Intestinal inflammasome activation in *Ube2o*$^{\Delta IEC}$ and *Ube2o* $^{f/f}$ mice.
(E and F) IL-18 ELISA of explants from *Ube2o*$^{\Delta IEC}$ (E) or *Nlrp6*^{DKR} (F) mice and littermate controls.
(G and H) Inflammasome activation (G) and IL-18 ELISA of explants (H) from untreated or AsIII-treated mice (intragastric, i.g.).
(I) Inflammasome activation in intestinal tissues from untreated, ATRA-treated (intravenous [i.v.]), or AsIII-treated (i.v.) mice.
(J and K) Representative mucus immunofluorescence images and quantification of mucus layer thickness. Scale bars, 50 μm.
(L) Representative SEM images of the indicated mice. Scale bars, 100 and 50 μm.
(M and N) ELISA of serum (M) and fecal (N) IL-18 from patients post therapy with AsIII and ATRA and from healthy controls.
(O) Summary diagram of monoubiquitination-driven NLRP6 inflammasome activation.
Data in (B)–(K) represent ≥3 experiments. Blue, red, and yellow asterisks indicate unmodified, single-monoubiquitinated, and multi-monoubiquitinated NLRP6, respectively. Data in (E), (F), (H), (K), (M), and (N): are shown as mean ± SEM. Two-group comparisons were performed using Student's *t* tests (ns, $*p < 0.05$, $**p < 0.01$, $***p < 0.001$, $**p < 0.0001$).
See also Figure S4.

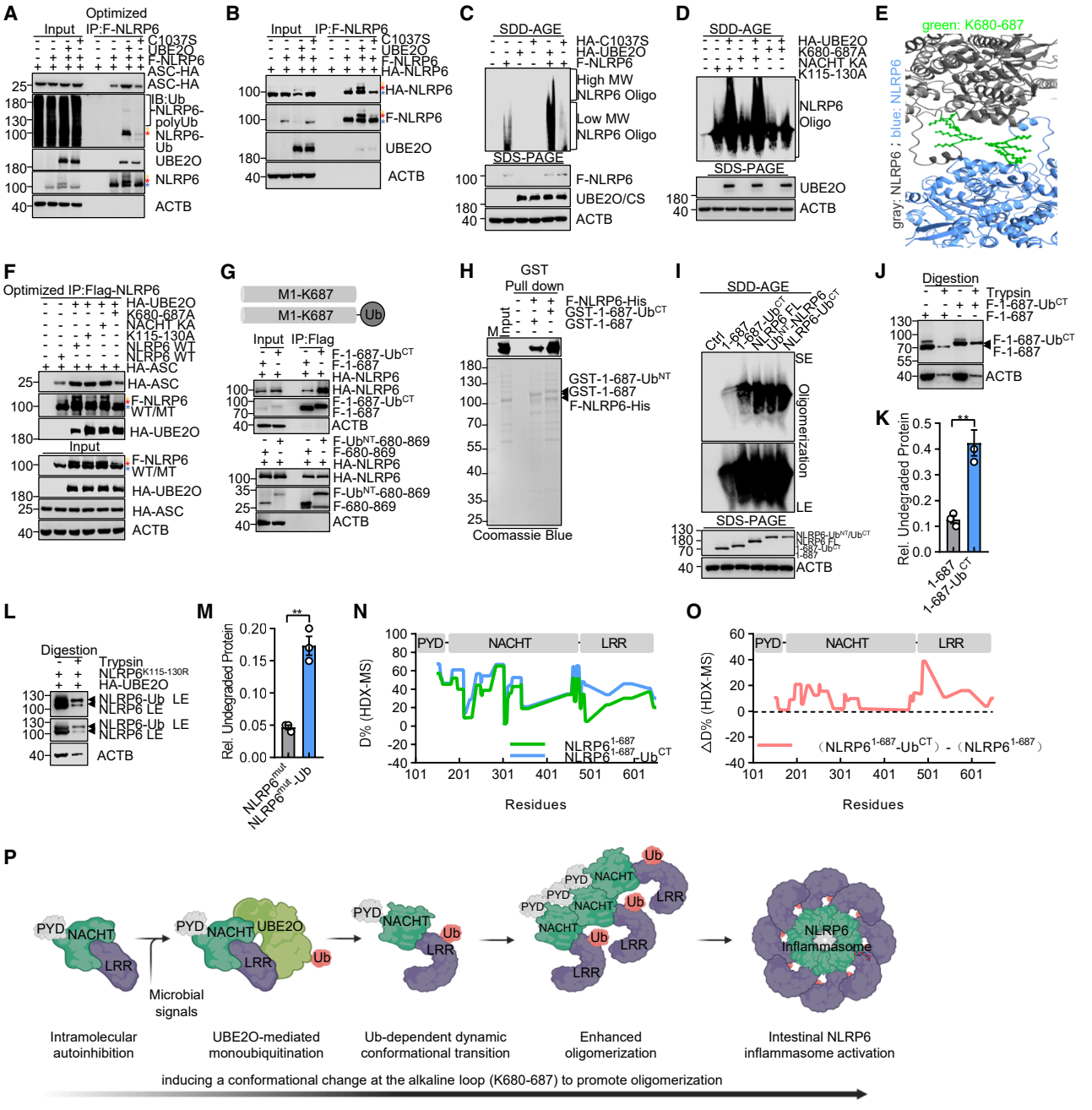

Figure 5. NLRP6 monoubiquitination at K680–687 facilitates its oligomerization through conformational transitions within the NACHT and LRR domains

(A) Optimized co-IP of NLRP6 and ASC in HEK293T cells transfected with indicated plasmids.
(B) Western blotting of NLRP6 self-binding in cells transfected with the indicated plasmids.
(C) Cellular NLRP6 oligomerization assessed by SDD-AGE in cells transfected with the indicated plasmids.
(D) Cellular NLRP6 oligomerization assessed by SDD-AGE in cells transfected with NLRP6 mutants and UBE2O.
(E) Representative predicted structure of two NLRP6 molecules generated by AlphaFold.
(F) Optimized co-IP of NLRP6/NLRP6 mutants with ASC in HEK293T cells co-expressing UBE2O.
(G) Self-binding of K680- and K687-monoubiquitination mimics in cells.
(H) *In vitro* binding assay between NLRP6$^{1–687}$-Ub^{CT} or NLRP6$^{1–687}$ and NLRP6.
(I) Cellular NLRP6 oligomerization assessed by SDD-AGE in cells transfected with the indicated plasmids.
(J and K) Degradation of NLRP6$^{1–687}$, NLRP6$^{1–687}$-Ub^{CT} treated with trypsin (J), and quantification of NLRP6 (K).
(L and M) Degradation of unmodified full-length NLRP6$^{K115–130R}$ and monoubiquitinated NLRP6$^{K115–130R}$ targeted by UBE2O treated with trypsin (L), and quantification of NLRP6 (M).
(N) HDX-MS analysis of NLRP6$^{1–687}$ and NLRP6$^{1–687}$-Ub^{CT}.

(legend continued on next page)

and initiated ASC filaments to form multiple bundles of varying thickness, and initiated cell death-mediated LDH release (Figures 3H–3L). Furthermore, UBE2O neither binds to nor regulates the inflammasome activity of NLRP3 or NLRP9 (Figures 1S and S3T–S3X). These results demonstrate that UBE2O regulates NLRP6 inflammasome activation *in vitro* (Figure 3M).

Monoubiquitination determines NLRP6 inflammasome activation *in vivo*

UBE2O deletion (*Ube2o*$^{\Delta IEC}$) or loss of NLRP6 monoubiquitination (*Nlrp6*^{DKR}) (Figure 4A) suppressed NLRP6 monoubiquitination and inflammasome activation, as evidenced by decreased Casp1 and GSDMD cleavage in IECs and intestinal tissues, as well as reduced interleukin (IL)-18 secretion (Figures 1Y, 4B–4F, and S4A–S4G). Intravenous or oral administration of AsIII also led to similar observations (Figures 4G–4I and S4H). Mucus secretion from goblet cells is maintained by NLRP6-activated GSDMD pores.[4,32] We observed impaired mucus secretion, with phenotypes of much thinner mucus layer and numerous protruding granules, in the colonic epithelium of *Nlrp6*^{KO}, *Ube2o*$^{\Delta IEC}$, and *Nlrp6*^{DKR} mice (Figures 4J–4L).

We also analyzed serum and fecal samples from six APL patients treated with intravenous ATO and all-*trans* retinoic acid (ATRA), which is the first-line treatment for acute APL.[33] Although a pre-treatment serum sample was available from only a single patient, previous studies have shown no significant differences in IL-18 levels between APL patients and healthy controls (HCs).[34] We therefore conducted comparative analyses between five additional patients and HCs, while performing a longitudinal comparison for the single case (Table S1). Markedly decreased IL-18 levels were detected in both serum and fecal samples (Figures 4M and 4N). Longitudinal assessment further identified time-dependent suppression of NLRP6 inflammasome activation, with significant IL-18 downregulation emerging at day 2 after daily ATO administration (Figures S4I and S4J). Together, these data demonstrate that NLRP6 monoubiquitination mediated by UBE2O determines inflammasome activation and links arsenic-induced gastrointestinal side effects to functional impairment of NLRP6 (Figure 4O).

NLRP6 monoubiquitination at K680–687 facilitates its oligomerization through conformational transition within NACHT and LRR domains

We next tested several activation processes related to the PYD and LRR domains. UBE2O promoted NLRP6-ASC binding in optimized coimmunoprecipitation (co-IP) systems (Figures 5A, S5A, and S5B), as well as NLRP6 self-binding and oligomerization, in an enzyme activity-dependent manner (Figures 5B and 5C). Notably, monoubiquitination at K680–687, but not at K115–130R, affected NLRP6 oligomerization (Figure 5D). AlphaFold analysis indicates that two NLRP6 molecules establish intermolecular interactions between alkaline loops (K680–K687) and the partial NAIP, CIITA, HET-E, and TP1 (NACHT) domain. This contrasts sharply with the reported oligomeric structures of mouse/human NLRC4 or NLRP3, which are stabilized by strong LRR- and NACHT-mediated interactions driving activation.[35] These findings suggest that NLRP6 may require large-scale intramolecular conformational changes to assemble into ordered oligomers mediated by the NACHT or LRR domains (Figures 5E and S5C–S5G). K680–687A mutation inhibited the monoubiquitination-enhanced NLRP6-ASC association, whereas K115–130A mutation did not affect NLRP6-mediated ASC recruitment (Figure 5F). These findings suggest that monoubiquitination at K680–687 facilitates NLRP6 oligomerization and subsequent ASC binding, thereby activating the NLRP6 inflammasome.

Ub mimics have been proven useful for directly investigating the functional roles and molecular mechanisms of ubiquitination.[36] To directly investigate the molecular mechanism of monoubiquitination at K680–687, we engineered two Ub-fusion constructs (NLRP6$^{1–687}$-Ub^{CT} and Ub^{NT}-NLRP6$^{680–869}$, in brief, implying a Ub attached to K687 or K680 with peptide bond) which sterically mimic K680–687 monoubiquitination (i.e., a Ub attached to the ε-amino group of K687 or K680 with isopeptide bond). These Ub-fusion mimics did not alter NLRP6 subcellular localization or protein levels compared with WT NLRP6 (Figures S5H and S5I). The ubiquitination mimic at K687 promoted NLRP6 N-terminal self-association, whereas modification at K680 had no effect on C-terminal self-interaction (Figure 5G). The mimic showed enhanced direct NLRP6 self-association *in vitro* and oligomerization in cells, whereas full-length NLRP6 with N- or C-terminal Ub fusions showed no effect on oligomerization, indicating that monoubiquitination-induced oligomerization is dependent on the K680–687 region (Figures 5H and 5I). These data demonstrate that the mimic effectively recapitulates UBE2O-mediated physiological monoubiquitination.

A trypsin-sensitive assay has been used to compare protein-folding tightness, which indirectly reflects conformational alterations.[37–39] UBE2O-mediated monoubiquitination at K680–687 or monoubiquitination mimic at K687 inhibited NLRP6 degradation, suggesting a more dynamic NLRP6 structure (Figures 5J–5M and S5J). Hydrogen/deuterium exchange MS (HDX-MS) has emerged as a robust method to study solution-phase protein dynamics directly perturbed by different binding events, such as those by chemical ligands, nucleic acids, or PTMs.[40] Data from purified NLRP6$^{1–687}$ and NLRP6$^{1–687}$-Ub^{CT} showed that the mimic induces significant conformational alterations by enhancing dynamics within both the NACHT and LRR domains (NACHT: L198–D216, S225–A230, R241–L272, Q312–A342; LRR: K465–F495, H537–F544, V577–E597, R632–L653) (Figures 5N and 5O). Conformational changes in the NACHT and/or LRR domains are necessary for the activation of NLRs.[35] The residues affected in HDX-MS of NLRP6$^{1–687}$-Ub^{CT} map to the LRR-NACHT interaction interface, including

(O) Comparative HDX-MS analysis of NLRP6$^{1–687}$ and NLRP6$^{1–687}$-Ub^{CT}.
(P) Schematic diagram illustrating NLRP6 inflammasome activation driven by K680–687 monoubiquitination.
Data in (A)–(D) and (F)–(O) represent ≥3 experiments. Blue, red, and yellow asterisks indicate unmodified, single-monoubiquitinated, and multi-monoubiquitinated NLRP6, respectively. Data in (K) and (M) are shown as mean ± SEM. Two-group comparisons were performed using Student's *t* tests (ns, $^{*}p < 0.05$, $^{**}p < 0.01$, $^{***}p < 0.001$, $^{**}p < 0.0001$).
See also Figure S5.

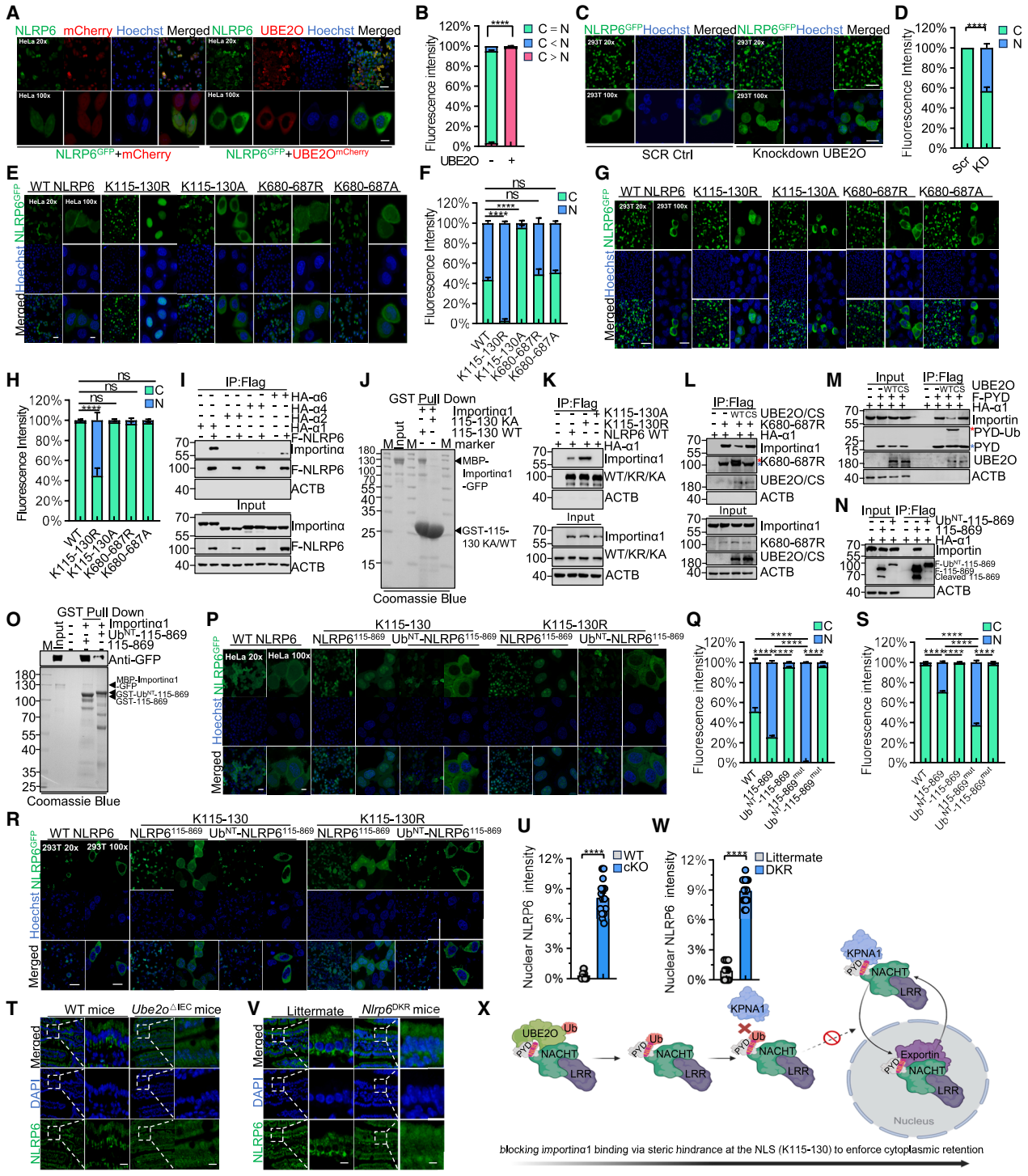

Figure 6. NLRP6 monoubiquitination at NLS$^{K115–130}$ inhibits NLS-importinα1 association through steric hindrance and facilitates NLRP6 cytoplasmic sequestration

(A and B) Representative images of HeLa cells stably transfected with mCherry-EV (empty vector) or UBE2O-mCherry with NLRP6-GFP (A), and statistics (B).

(C and D) Representative images of HEK293T cells stably transfected with NLRP6-GFP with lentiviruses expressing either control short hairpin RNA (shRNA) or UBE2O shRNA (C), and statistics (D).

(E and F) Representative images of HeLa cells stably transfected with the indicated NLRP6 mutants (E), and statistics (F).

(G and H) Representative images of HEK293T cells stably transfected with the indicated NLRP6 mutants (G), and statistics (H).

(I) Co-IP validation of interactions between NLRP6 and importinα proteins identified by LC-MS/MS.

(J) *In vitro* binding between K115–130 or mutant peptides and importinα1.

(legend continued on next page)

L198–D216, R241–L272, and Q312–A342 in the NACHT, as well as K465–F495, H537–F544, and R632–L653 in the LRR. Consistent with this, AlphaFold predictions indicate that monoubiquitination mimicked at K687 induces conformational rearrangements within monomeric NLRP6 (residues 1–687) and remodels the dimerization interface between two NLRP6 molecules (Figures S5K and S5C–S5G). These data suggest that monoubiquitination at K680–687 induces conformational remodeling in the NACHT and LRR domains to facilitate NLRP6 oligomerization (Figure 5P).

NLRP6 monoubiquitination at NLS$^{K115–130}$ inhibits NLS-importinα1 association through steric hindrance and facilitates NLRP6 cytoplasmic sequestration

It is intriguing how monoubiquitination at NLRP6 K115–130 contributes to inflammasome activation, because it does not affect ASC recruitment or NLRP6 oligomerization (Figures 3E, 5D, and 5F). NLRP6 is almost exclusively localized in the cytoplasm in HEK293T cells but is evenly distributed in HeLa cells, and UBE2O is differentially expressed between these two cell lines (Figures S6A–S6C). Thus, we suspect that NLRP6 monoubiquitination may contribute to its subcellular localization. Indeed, co-expression of NLRP6 and UBE2O in HeLa cells reduced the nuclear localization of NLRP6 (Figures 6A and 6B), whereas knockdown of UBE2O in HEK293T cells increased nuclear localization (Figures 6C, 6D, and S6D–S6G). We therefore speculated that UBE2O may target NLRP6 lysines near or within NLS to regulate its nuclear translocation.

Using the NLStradam tool, we found that there are two NLS sequences, NLS1 (K115–F143) and NLS2 (K680–K697), which coincidently cover the two poly-lysine regions (K115–130 and K680–687) modified by UBE2O (Figure S6H). We next tested whether these two NLSs are required for NLRP6 nuclear translocation using K-to-A mutation (disrupting the NLS due to alterations in side-chain structure and charge), and also tested whether monoubiquitinations at these two NLSs affects NLRP6 nuclear localization using K-to R-mutations (lysine-like side-chain architecture and charge, mimicking the intact but monoubiquitination-resistant NLS) (Figure S6I). Due to low expression of UBE2O in HeLa cells, approximately half GFP-fused WT NLRP6 was distributed in the cytoplasm. The NLRP6$^{K680–687A}$ mutants did not affect the NLRP6 distribution, whereas the NLRP6$^{K115–130A}$ mutants were completely sequestered in the cytoplasm. The GFP-fused NLRP6$^{K680–687R}$ mutants also did not affect the distribution, whereas the NLRP6$^{K115–130R}$ mutants were completely sequestered in the nucleus (Figures 6E, 6F, S6J, and S6K). Due to high expression of UBE2O in HEK293T cells, almost all GFP-fused WT NLRP6 was distributed in the cytoplasm, approximately half of the NLRP6$^{K115–130R}$ mutants were distributed in the nucleus, whereas all other three mutants did not affect the NLRP6 distribution (Figures 6G, 6H, S6L, and S6M). Further, the distributions of NLRP6 and its mutants in intestinal epithelial cell lines (CT26 and HCT116) were similar to those observed in HEK293T cells (Figures S6N–S6Q). These data suggest NLS1 mainly mediated the NLRP6 nucleic translocation and that monoubiquitination of lysines in NLS1 prevents nuclear translocation.

Importins are known to interact with NLSs to mediate protein nuclear translocation. We performed IP/MS by transfecting FLAG-NLRP6^{PYD} into HEK293T cells or by incubating purified glutathione S-transferase (GST)-NLRP6 with IECs lysates, and found that importinα1 was one of the top hits in both assays (Figures S6R and S6S). Among these importins, importinα1 showed a strong interaction with NLRP6, whereas importinα6 showed a weak interaction with NLRP6 (Figure 6I). Notably, AlphaFold predication also suggested a strong interaction between NLRP6 NLS (K115–130) and the importinα1 ARM domain (Figures S6T and S6U), which is known to interact with NLS.[41]

Direct binding between the NLS peptide (115-KKKYREHVLRQHAKVK-130) and importinα1 was validated *in vitro*, whereas either Ub fusion or NLS mutation abolished NLS-importinα1 binding (Figures 6J and S6V). Disruption of the NLRP6 NLS (K115–130A) inhibited its interaction with importinα1, whereas removal of monoubiquitination from the NLS (K115–130R) enhanced its interaction with importinα1 (Figures 6K, S6W, and S6X). Consistently, UBE2O also suppressed both NLRP6-importinα1 and NLRP6^{PYD}-importinα1 interactions (Figures 6L and 6M). These findings demonstrate that UBE2O directly targets the NLRP6 NLS (K115–130) motif and prevents importinα1 from recognizing the NLS through monoubiquitination.

We then investigated the consequence of monoubiquitination at K115–130 by engineering an N-terminal Ub-fusion construct (Ub^{NT}-NLRP6$^{115–869}$) to sterically mimic K115–130 monoubiquitination. Ub^{NT}-NLRP6$^{115–869}$ displayed reduced importinα1 binding both in cells and *in vitro* (Figures 6N and 6O). Notably, the Ub fusion completely blocked nuclear localization of NLRP6$^{115–869}$. Although the Ub^{NT}-NLRP6$^{115–869/K115–130R}$ mutant (monoubiquitination-resistant but with an intact NLS) exhibited enhanced nuclear localization (~60% in HEK293T

(K) Co-IP of NLRP6^{WT}, NLRP6$^{K115–130A}$, and NLRP6$^{K115–130R}$ with importinα1.
(L) Co-IP of modified or unmodified NLRP6$^{K680–687R}$ with importinα1.
(M) Co-IP of modified or unmodified PYD at K115-130 with importinα1.
(N) Co-IP of the K115-monoubiquitination mimic with importinα1.
(O) *In vitro* binding of the K115-monoubiquitination mimic with importinα1.
(P and Q) Representative images of HeLa cells stably transfected with GFP-tagged K115-monoubiquitination mimic and mutants (P), and statistics (Q).
(R and S) Representative images of HEK293T cells stably transfected with GFP-tagged K115-monoubiquitination mimic and mutants (R), and statistics (S).
(T–W) Representative immunofluorescence images of proximal small intestine sections (T and V), and statistics (U and W).
(X) Schematic diagram illustrating the mechanism of NLRP6 inflammasome activation driven by monoubiquitination.
Scale bars, 10 and 50 μm in (A), (C), (E), (G), (P), and (R); 20 and 100 μm in (T) and (V). Data in (A)–(V) represent ≥3 experiments. Data in (B), (D), (F), (H), (Q), (S), (U), and (W) are shown as mean ± SEM. Two-group comparisons were performed using Student's *t* tests; comparisons of more than two groups were performed using ANOVA (ns, $^{*}p < 0.05$, $^{**}p < 0.01$, $^{***}p < 0.001$, $^{**}p < 0.0001$).
See also Figure S6.

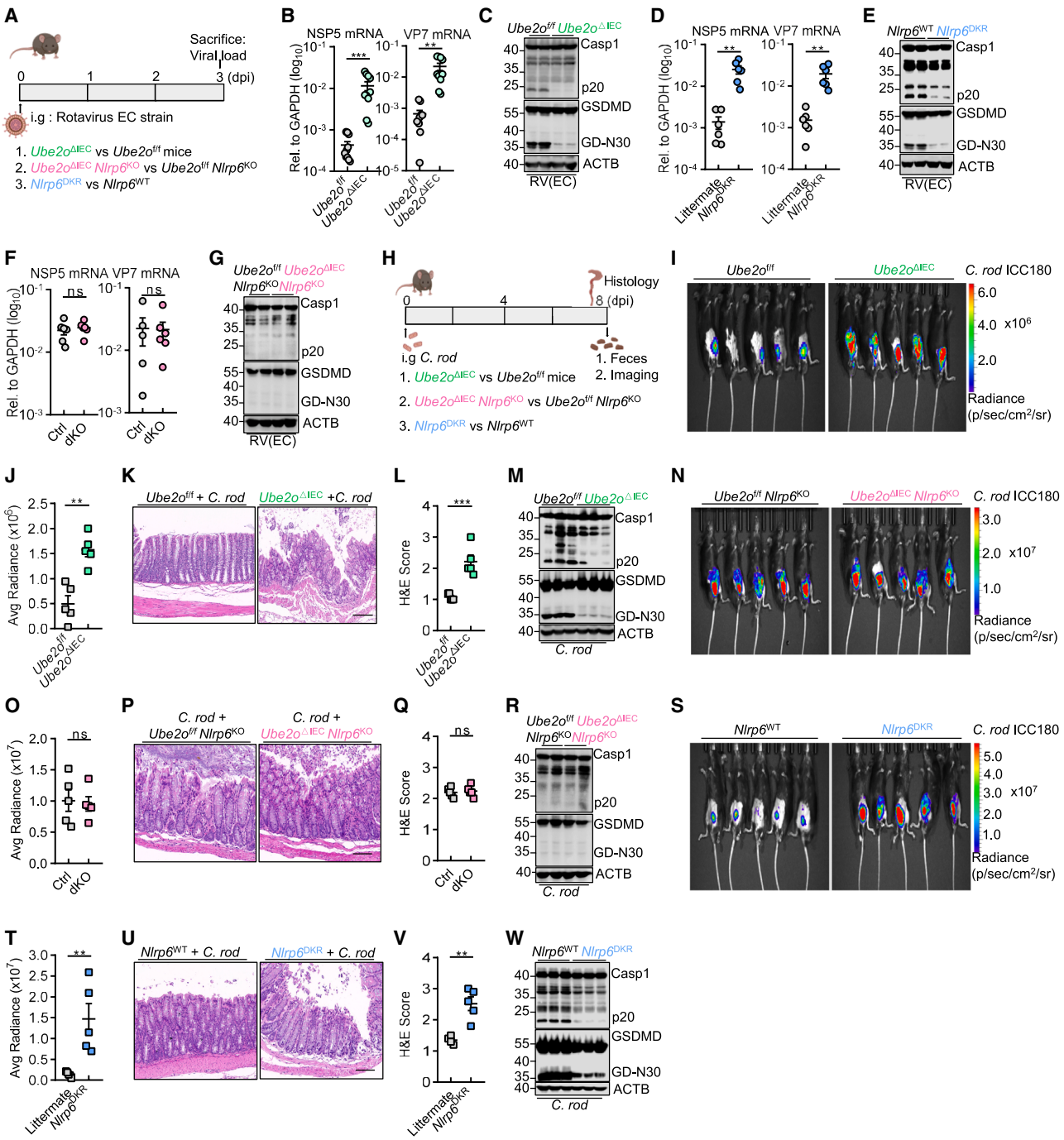

Figure 7. *Ube2o*$^{\Delta IEC}$ and *Nlrp6*^{DKR} mice exhibit impaired NLRP6 inflammasome activation and defense against *C. rodentium* and RV infection

(A) Schematic diagram of RV (EC strain) infection model.
(B) Quantitative real-time PCR analysis of viral loads in the jejunum from the indicated mice.
(C) Inflammasome activation in tissues from the indicated mice post infection.
(D) Quantitative real-time PCR analysis of viral loads in the jejunum from the indicated mice.
(E) Inflammasome activation in tissues post infection.
(F) Quantitative real-time PCR analysis of viral loads in the jejunum from the indicated mice.
(G) Inflammasome activation in tissues post infection.
(H) Schematic diagram of the bioluminescent *C. rodentium* infection model.
(I and J) *In vivo* optical imaging of *C. rodentium* and statistics.
(K and L) H&E staining of the indicated mice post infection (K), and histological scores (L). Scale bars, 100 μm.
(M) Inflammasome activation in tissues post infection.

(legend continued on next page)

and 100% in HeLa), the nuclear import process was impeded by Ub fusion at K115 (Figures 6P–6S), which is consistent with results from the NLRP6$^{K115–130A}$ mutant (Figures 6E and 6G). Intriguingly, NLRP6$^{115–869}$ localizes more to the nucleus (even the nucleolus), compared with full-length NLRP6 in both HEK293T and HeLa cells (~0% WT NLRP6 or 30% NLRP6$^{115–869}$ in HEK293T; ~50% WT NLRP6 or 80% NLRP6$^{115–869}$ in HeLa), suggesting that the NLRP6 N-terminal 1–114 sequence has an autoinhibition function for NLS-importinα1 binding and subsequent nuclear translocation (Figures 6P and 6R). Furthermore, data from trypsin-sensitive assays and HDX-MS showed that the monoubiquitination mimic had no effect on conformational changes, which is consistent with AlphaFold prediction (Figures S6Y–S6C′). Moreover, NLRP6 was mainly distributed in the cytoplasm of the villus cells in the small intestine, whereas in *Ube2o*$^{\Delta IEC}$, and *Nlrp6*^{DKR} mice, which lack NLRP6 monoubiquitination, the nuclear distribution of NLRP6 was robustly increased (Figures 6T–6W, S6D′, and S6E′).

Together, these results demonstrate that NLRP6 monoubiquitination at K680–687 facilitates its oligomerization through conformational changes, whereas monoubiquitination at K115–130 inhibits NLS-importinα1 binding through steric hindrance, thereby sustaining NLRP6 cytoplasmic sequestration. These two monoubiquitination events enable NLRP6 to efficiently assemble the inflammasome complex and mediate downstream signaling in the cytoplasm (Figures 5P and 6X).

Monoubiquitination maintains NLRP6-dependent defense against RV infection

Since NLRP6 inflammasome activation is reported to participate in antimicrobial defense,[4,9] we tested the role of NLRP6 monoubiquitination in enteric bacterial and viral infection models. We evaluated the effects of UBE2O and NLRP6 monoubiquitination in a RV (EDIM-Cambridge strain [EC strain]) infection model. Both *Ube2o*$^{\Delta IEC}$ and *Nlrp6*^{DKR} mice showed higher viral loads in the intestine and MLN than littermate controls (Figures 7A, 7B, 7D, S7A, and S7B; Table S3). These mice also exhibited impaired NLRP6 inflammasome activation, suggesting that lack of monoubiquitinase or monoubiquitination of NLRP6 leads to impaired inflammasome activation and uncontrolled RV infection (Figures 7C and 7E; Table S3). Moreover, no difference in viral load or inflammasome activation was observed in the intestine from *Ube2o*$^{\Delta IEC}$ *Nlrp6*^{KO} mice compared with *Ube2o*$^{f/f}$ *Nlrp6*^{KO} mice (Figures 7F, 7G, and S7C; Table S3). Since NLRP6 is reported to exert antiviral functions through both inflammasome-dependent and inflammasome-independent (IFN) pathways.[6,7,9] We quantified serum IFN-β levels via ELISA and assessed the expression profiles of ISGs during early infection to avoid the influence of differences in viral load. No difference in ISGs transcription or IFN-β secretion was observed, demonstrating that NLRP6 monoubiquitination did not affect IFN pathways (Figures S7D–S7J; Table S3).

Monoubiquitination maintains NLRP6-dependent defense against *C. rodentium* infection

Upon exposure of these mice to *C. rodentium*, bacterial numbers increased significantly in the lumen and feces of *Ube2o*$^{\Delta IEC}$ mice compared with littermate controls (Figures 7H–7J and S7K–S7N). *Ube2o*$^{\Delta IEC}$ mice exhibited shortened colon length, increased immune cells infiltrations, and impaired NLRP6 inflammasome activation compared with littermates, suggesting that lack of monoubiquitinase activity toward NLRP6 leads to impaired NLRP6 inflammasome activation and uncontrolled *C. rodentium* infection (Figures 7K–7M, S7O, and S7P). Notably, further depletion of NLRP6 abolished this phenotype, as no difference in antibacterial parameters was observed, suggesting that UBE2O primarily relied on NLRP6 to resist *C. rodentium* infection (Figures 7N–7R and S7Q–S7V). Further, consistent with the phenotype in *Ube2o*$^{\Delta IEC}$ mice, we observed significantly increased fecal bacterial load, shortened colon length, more severe mucosal pathologic features, and impaired inflammasome activation in *Nlrp6*^{DKR} mice (Figures 7S–7W and S7W–S7B′).

In summary, these data demonstrate that UBE2O-mediated monoubiquitination at K115–130 and K680–687 cooperatively determines NLRP6 inflammasome-dependent antimicrobial immunity (Figure S8).

DISCUSSION

PTMs are required for the activation of NLRP6 inflammasome

PTMs such as phosphorylation, ubiquitination, and cleavage determine the activation of PRRs, including TLRs, CD39-like nucleoside triphosphate diphosphohydrolase (CD-NTpase), RIG-I-like receptors (RLRs), C-type lectin receptors (CLRs), and NOD-like receptors (NLRs)[11,12,14–18,42] in response to PAMPs or DAMPs. However, under steady state, these sensors, expressed in immune cells, typically show minimal or no activation, as their PTMs are either absent or kept at low levels, and their expression is maintained at a low threshold to prevent unnecessary immune responses. This ensures that the immune system remains poised but not overly reactive in the absence of infection or danger signals. The intestine constantly faces a complex array of stimuli. It is essential to maintain sustained NLRP6 inflammasome activation in response to commensal microbes while also allowing inducible activation to respond to potential infections, thereby modulating both basal immune

(N and O) *In vivo* optical imaging of *C. rodentium* and statistics in the indicated mice.
(P and Q) H&E staining of the indicated mice post infection (P), and histological scores (Q). Scale bars, 100 μm.
(R) Inflammasome activation in tissues post infection.
(S and T) *In vivo* optical imaging of *C. rodentium* and statistics in the indicated mice.
(U and V) H&E staining of the indicated mice post infection (U), and histological scores (V). Scale bars, 100 μm.
(W) Inflammasome activation in tissues post infection.
Data in (B)–(G) and (I)–(W) represent ≥3 experiments. Data in (B), (D), (F), (H), (J), (L), (O), (Q), (T), and (V) are shown as mean ± SEM. Two-group comparisons were performed using Student's *t* tests (ns, $*p < 0.05$, $**p < 0.01$, $***p < 0.001$, $**p < 0.0001$).
See also Figure S7.

surveillance and timely immune defense required for intestinal homeostasis. Here, we found that UBE2O-mediated monoubiquitination determines NLRP6 inflammasome activation. Loss of NLRP6 monoubiquitination due to UBE2O deficiency or NLRP6 mutations results in impaired inflammasome activation under both physiological and pathological conditions. Our study provides evidence that monoubiquitination acts as a critical regulatory mechanism for NLRP6 inflammasome activation in the gut. This previously unrecognized pathway operates through site-specific monoubiquitination at both the PYD and LRR domains. It remains unclear whether other canonical NLR receptors undergo monoubiquitination during inflammasome activation and which microbial signals initiate the UBE2O-NLRP6 axis.

New understandings of monoubiquitination-mediated signal transduction

In cellular signal transduction, K48-linked and K63-linked polyubiquitination have been well characterized for their critical roles in modulating signal activation by regulating protein degradation and conformational changes at different scales, thereby influencing the fate of cells and organisms. However, research on monoubiquitination remains comparatively sparse.

(1) Functional distinctions: unlike polyubiquitination, which has been linked to protein-protein interaction and degradation, monoubiquitination has largely been linked to chromatin regulation, protein sorting, complex assembly, and trafficking through covalent conjugation to a lysine residue of the substrate, suggestive of its suitability for large macromolecular complexes. (2) Different enzymes: there are ~700 UMEs encoded by the human genome, but only a small number possess monoubiquitination activity (UBE2O, PRC1, RNF40, Cullin3, TRIM56, TRIM41, MDM2, TIF1γ, NEDD4, SKP2, HOIL-1L, RNF8, UBE2T, FANCL, and RSP5) or de-monoubiquitination activity (ASXL1, BAP1, USP7, UBP2, USP4, USP9X, and USP1). (3) Molecular size and local impact: the diameter of polyubiquitination depends on the type and length of the chain, typically exceeding tens of nanometers, whereas a single Ub molecule has a diameter of ~4.5 nm. The smaller size of a single Ub molecule allows it to induce more flexible structural changes compared with polyubiquitination, making it particularly suited for the conformational changes in macromolecular complexes. (4) Dual mechanism vs. single mechanism: due to differences in group diameter and modified sites, polyubiquitination typically functions through a single mechanism that depends on either a single site or a single region. In contrast, monoubiquitination can occur at distant lysines on the substrate, even spanning across two separate domains, to mediate a multifunctionality, which adds a layer of complexity to the regulatory network. This indicates that each ubiquitination site can modulate the protein's behavior in a context-dependent manner, providing a more flexible regulatory framework compared with polyubiquitination.

Double assurance of inflammasome activation by regulating both oligomerization and cytoplasmic sequestration

One often overlooked aspect is that cytoplasmic sensors need to be maintained in the cytoplasm, which is essential for the subsequent activation. How NLRP6, previously considered a cytosolic sensor, is confined to the cytoplasm remains completely unknown. The UBE2O-targeted K115–K130 region (KKKYREHVLRQHAKVK), which contains the consensus sequence of bipartite NLS (R/K(X)$_{10–12}$KRXK), constitutes the NLS of NLRP6. Monoubiquitination at K115–130 blocks NLRP6-importinα1 interaction through steric hindrance, thereby synergizing with monoubiquitination at K680–687 to promote NLRP6 oligomerization through conformational changes, which subsequently activates the inflammasome pathway. This dual-assurance mechanism fundamentally distinguishes NLRP6 inflammasome activation from the post-translational regulatory mechanisms of other NLRs. Synergistic monoubiquitination of both the PYD and LRR domains is required for NLRP6 inflammasome activation. The structure of NLRP3 indicates that conformational changes in both the PYD and LRR domains are essential for inflammasome activation.[43,44] It remains unknown whether NLRP3 and other NLRs undergo nuclear exclusion and, if so, how such a mechanism regulates their inflammasome activation. Nuclear cGAS suppresses DNA repair and promotes tumorigenesis.[45] Exploring the nuclear functions of NLRP6 will be an important direction for future investigation.

Divergent activation dynamics of the NLRP6 or NLRP3 inflammasomes

The differential regulation of NLRP6 in IECs vs. NLRP3 in myeloid cells underscores a nuanced understanding of inflammasome activation. Unlike the NLRP3 inflammasome in myeloid cells, which requires transcriptional upregulation of NLRP3 as a priming signal followed by assembly in response to PAMPs and DAMPs, NLRP6 activation is driven by infection-induced monoubiquitination at the post-translational level, specifically on constitutively expressed NLRP6. Inducibly expressed NLRP3 in immune cells primarily faces a sterile environment and needs to be activated in response to chronic inflammation. Transcriptional upregulation and translation of NLRP3, on a timescale of hours, reflect a more static yet potent mechanism to handle systemic inflammation. In contrast, NLRP6, which is predominantly and constitutively expressed in IECs, faces complex and varied challenges in the intestinal lumen and requires more dynamic regulation. Therefore, the PTMs of constitutively expressed NLRP6, occurring on a timescale of minutes, exert a dynamic and adaptable response tailored to the gut environment.

Implications of NLRP6 monoubiquitination for human health

Small-molecule inhibitors of the NLRP3 inflammasome that are now in clinical trials have demonstrated proof of concept that inflammasomes are druggable, and drug development programs are now focusing on other key inflammasome molecules.[46] As a sensor that is predominantly expressed in IECs, NLRP6 mediates multiple signals, including inflammasome and IFN pathways in the gut, and mediates multiple functions in host defense, inflammation, and barrier function.

Arsenicals, such as ATO, AsIII, and realgar-Indigo naturalis formula (RIF) are the first-line treatments for APL in the clinic. However, the treatment of newly diagnosed patients with arsenicals and the management of side effects remains challenging, which limits their clinical application in complex acute myeloid leukemia (AML).[33,47–49] Treatment of leukemia patients with

arsenicals and long-term antimicrobial prophylaxis leads to gut dysbiosis, barrier dysfunction, and increased infectious risk, accompanied by abdominal pain, diarrhea, constipation, dyspepsia, and loose stools.[33] We found that the UBE2O-NLRP6 axis is evolutionarily conserved across species, including humans and mice, due to sequence conservation in UBE2O and residue conservation in NLRP6. Moreover, intravenous administration of arsenicals inhibits NLRP6 inflammasome activation in both human samples and mouse models, highlighting the potential influence of arsenicals in modulating the intestinal immunity.

Limitations of the study

Two aspects remain unclear: (1) structural details of the UBE2O-NLRP6 complex underlying the effect of monoubiquitination on NLRP6 oligomerization remain elusive; and (2) the upstream microbial signal(s) that induce the UBE2O-mediated NLRP6 monoubiquitination remain unknown.

RESOURCE AVAILABILITY

Lead contact

Further information and requests for resources and reagents should be directed to and will be fulfilled by the lead contact, Shu Zhu (zhushu@ustc.edu.cn).

Materials availability

Materials are available from the lead contact upon request.

Data and code availability

This paper does not generate original code. All additional information required to reanalyze the data reported in this paper is available from the lead contact upon request.

ACKNOWLEDGMENTS

We are grateful to Dr. Ramanujan S. Hegde from Cambridge University for providing UBE2O and mutant plasmids and to Dr. Youcun Qian from the Institute of Nutrition and Health, Shanghai, for providing ubiquitin-expressing plasmids. We thank Dr. Anmin Wang for the suggestions on viral infections and Mengjie Liu for helping with mouse genotyping and maintenance. This work was supported by grants from the National Key R&D Program of China (2023YFC2306101) (S.Z.), the National Natural Science Foundation of China (82325025, 82588302, 82341121, 92374204 to S.Z. and 32400720 to D.W.), the Strategic Priority Research Program of the CAS (XDB0940303) (R.L.), the Fundamental and Interdisciplinary Disciplines Breakthrough Plan of the Ministry of Education of China (JYB2025XDXM506) (R.Z.), the CAS Project for Young Scientists in Basic Research (YSBR-074) (S.Z.), and the China Postdoctoral Science Foundation (2024M753129) (D.W.).

AUTHOR CONTRIBUTIONS

D.W. designed, performed, and interpreted most of the experiments. X.C. helped with cell culture and mouse experiments. K.S., R.L., and A.W. helped with cell culture experiments. R.Z contributed helpful discussions and provided materials. F.D., K.W., W.Z., X.Z., Y.H., and S.Y. collected the human samples. J.Z. conducted HDX-MS assay and contributed helpful discussions. D.W. and S.Z. wrote the manuscript. S.Z. supervised the project.

DECLARATION OF INTERESTS

S.Z. is a cofounder of Ibiome, which studies microbial regulation of immune responses.

STAR★METHODS

Detailed methods are provided in the online version of this paper and include the following:

- KEY RESOURCES TABLE
- EXPERIMENTAL MODEL AND STUDY PARTICIPANT DETAILS
  - Human samples
  - Mice
  - Citrobacter rodentium infection model in mice
  - Rotavirus infection model in mice
  - Cell lines, transfection, and cell sorting
  - Isolation of IECs and IELs in the intestine
- METHOD DETAILS
  - Protein expression
  - GST-tag protein purification with FPLC from *E. coli* BL21
  - His-tag protein purification with FPLC from 293F
  - GST pull-down, immunoprecipitation, and immunoblotting
  - HDX-MS
  - Trypsin sensitivity assay
  - Optimized ASC-NLRs immunoprecipitation
  - IP-LC-MS/MS
  - Ubiquitination assay
  - RNA interference
  - ELISA
  - Inflammasome reconstruction system in cells
  - ASC oligomerization assay
  - ASC filaments
  - LDH release assay
  - SDD-AGE assay
  - Nuclear and cytoplasmic isolation assay
  - RNA isolation, quantitative real-time PCR, and primers
  - Immunofluorescence and live-cell imaging by confocal microscopy
- QUANTIFICATION AND STATISTICAL ANALYSIS

SUPPLEMENTAL INFORMATION

Supplemental information can be found online at https://doi.org/10.1016/j.chom.2025.12.009.

Received: January 21, 2025
Revised: September 2, 2025
Accepted: December 11, 2025
Published: January 6, 2026

REFERENCES

1. Carpenter, S., and O'Neill, L.A.J. (2024). From periphery to center stage: 50 years of advancements in innate immunity. Cell *187*, 2030–2051. https://doi.org/10.1016/j.cell.2024.03.036.
2. Barnett, K.C., Li, S., Liang, K., and Ting, J.P.Y. (2023). A 360° view of the inflammasome: Mechanisms of activation, cell death, and diseases. Cell *186*, 2288–2312. https://doi.org/10.1016/j.cell.2023.04.025.
3. Elinav, E., Strowig, T., Kau, A.L., Henao-Mejia, J., Thaiss, C.A., Booth, C.J., Peaper, D.R., Bertin, J., Eisenbarth, S.C., Gordon, J.I., et al. (2011). NLRP6 inflammasome regulates colonic microbial ecology and risk for colitis. Cell *145*, 745–757. https://doi.org/10.1016/j.cell.2011.04.022.
4. Wlodarska, M., Thaiss, C.A., Nowarski, R., Henao-Mejia, J., Zhang, J.P., Brown, E.M., Frankel, G., Levy, M., Katz, M.N., Philbrick, W.M., et al. (2014). NLRP6 inflammasome orchestrates the colonic host-microbial interface by regulating goblet cell mucus secretion. Cell *156*, 1045–1059. https://doi.org/10.1016/j.cell.2014.01.026.
5. Hara, H., Seregin, S.S., Yang, D., Fukase, K., Chamaillard, M., Alnemri, E.S., Inohara, N., Chen, G.Y., and Núñez, G. (2018). The NLRP6 Inflammasome Recognizes Lipoteichoic Acid and Regulates Gram-Positive Pathogen Infection. Cell *175*, 1651–1664.e14. https://doi.org/10.1016/j.cell.2018.09.047.

6. Shen, C., Li, R., Negro, R., Cheng, J., Vora, S.M., Fu, T.M., Wang, A., He, K., Andreeva, L., Gao, P., et al. (2021). Phase separation drives RNA virus-induced activation of the NLRP6 inflammasome. Cell *184*, 5759–5774.e20. https://doi.org/10.1016/j.cell.2021.09.032.

7. Li, R., Zan, Y., Wang, D., Chen, X., Wang, A., Tan, H., Zhang, G., Ding, S., Shen, C., Wu, H., et al. (2024). A mouse model to distinguish NLRP6-mediated inflammasome-dependent and -independent functions. Proc. Natl. Acad. Sci. USA *121*, e2321419121. https://doi.org/10.1073/pnas.2321419121.

8. Mukherjee, S., Kumar, R., Tsakem Lenou, E., Basrur, V., Kontoyiannis, D.L., Ioakeimidis, F., Mosialos, G., Theiss, A.L., Flavell, R.A., and Venuprasad, K. (2020). Deubiquitination of NLRP6 inflammasome by Cyld critically regulates intestinal inflammation. Nat. Immunol. *21*, 626–635. https://doi.org/10.1038/s41590-020-0681-x.

9. Wang, P., Zhu, S., Yang, L., Cui, S., Pan, W., Jackson, R., Zheng, Y., Rongvaux, A., Sun, Q., Yang, G., et al. (2015). Nlrp6 regulates intestinal antiviral innate immunity. Science *350*, 826–830. https://doi.org/10.1126/science.aab3145.

10. Liu, J., Qian, C., and Cao, X. (2016). Post-Translational Modification Control of Innate Immunity. Immunity *45*, 15–30. https://doi.org/10.1016/j.immuni.2016.06.020.

11. Chuang, T.H., and Ulevitch, R.J. (2004). Triad3A, an E3 ubiquitin-protein ligase regulating Toll-like receptors. Nat. Immunol. *5*, 495–502. https://doi.org/10.1038/ni1066.

12. Dai, J., Huang, Y.J., He, X., Zhao, M., Wang, X., Liu, Z.S., Xue, W., Cai, H., Zhan, X.Y., Huang, S.Y., et al. (2019). Acetylation Blocks cGAS Activity and Inhibits Self-DNA-Induced Autoimmunity. Cell *176*, 1447–1460.e14. https://doi.org/10.1016/j.cell.2019.01.016.

13. Xu, P., Liu, Y., Liu, C., Guey, B., Li, L., Melenec, P., Ricci, J., and Ablasser, A. (2024). The CRL5-SPSB3 ubiquitin ligase targets nuclear cGAS for degradation. Nature *627*, 873–879. https://doi.org/10.1038/s41586-024-07112-w.

14. Rehwinkel, J., and Gack, M.U. (2020). RIG-I-like receptors: their regulation and roles in RNA sensing. Nat. Rev. Immunol. *20*, 537–551. https://doi.org/10.1038/s41577-020-0288-3.

15. Cadena, C., Ahmad, S., Xavier, A., Willemsen, J., Park, S., Park, J.W., Oh, S.W., Fujita, T., Hou, F., Binder, M., et al. (2019). Ubiquitin-Dependent and -Independent Roles of E3 Ligase RIPLET in Innate Immunity. Cell *177*, 1187–1200.e16. https://doi.org/10.1016/j.cell.2019.03.017.

16. Mócsai, A., Ruland, J., and Tybulewicz, V.L.J. (2010). The SYK tyrosine kinase: a crucial player in diverse biological functions. Nat. Rev. Immunol. *10*, 387–402. https://doi.org/10.1038/nri2765.

17. Kesavardhana, S., Kuriakose, T., Guy, C.S., Samir, P., Malireddi, R.K.S., Mishra, A., and Kanneganti, T.D. (2017). ZBP1/DAI ubiquitination and sensing of influenza vRNPs activate programmed cell death. J. Exp. Med. *214*, 2217–2229. https://doi.org/10.1084/jem.20170550.

18. Swanson, K.V., Deng, M., and Ting, J.P.Y. (2019). The NLRP3 inflammasome: molecular activation and regulation to therapeutics. Nat. Rev. Immunol. *19*, 477–489. https://doi.org/10.1038/s41577-019-0165-0.

19. Popovic, D., Vucic, D., and Dikic, I. (2014). Ubiquitination in disease pathogenesis and treatment. Nat. Med. *20*, 1242–1253. https://doi.org/10.1038/nm.3739.

20. Dikic, I., and Schulman, B.A. (2023). An expanded lexicon for the ubiquitin code. Nat. Rev. Mol. Cell Biol. *24*, 273–287. https://doi.org/10.1038/s41580-022-00543-1.

21. Ge, W., Yu, C., Li, J., Yu, Z., Li, X., Zhang, Y., Liu, C.P., Li, Y., Tian, C., Zhang, X., et al. (2023). Basis of the H2AK119 specificity of the Polycomb repressive deubiquitinase. Nature *616*, 176–182. https://doi.org/10.1038/s41586-023-05841-y.

22. Yip, M.C.J., Sedor, S.F., and Shao, S. (2022). Mechanism of client selection by the protein quality-control factor UBE2O. Nat. Struct. Mol. Biol. *29*, 774–780. https://doi.org/10.1038/s41594-022-00807-6.

23. Yanagitani, K., Juszkiewicz, S., and Hegde, R.S. (2017). UBE2O is a quality control factor for orphans of multiprotein complexes. Science *357*, 472–475. https://doi.org/10.1126/science.aan0178.

24. Liang, K., Volk, A.G., Haug, J.S., Marshall, S.A., Woodfin, A.R., Bartom, E.T., Gilmore, J.M., Florens, L., Washburn, M.P., Sullivan, K.D., et al. (2017). Therapeutic Targeting of MLL Degradation Pathways in MLL-Rearranged Leukemia. Cell *168*, 59–72.e13. https://doi.org/10.1016/j.cell.2016.12.011.

25. Mashtalir, N., Daou, S., Barbour, H., Sen, N.N., Gagnon, J., Hammond-Martel, I., Dar, H.H., Therrien, M., and Affar el, B. (2014). Autodeubiquitination protects the tumor suppressor BAP1 from cytoplasmic sequestration mediated by the atypical ubiquitin ligase UBE2O. Mol. Cell *54*, 392–406. https://doi.org/10.1016/j.molcel.2014.03.002.

26. Vila, I.K., Yao, Y., Kim, G., Xia, W., Kim, H., Kim, S.J., Park, M.K., Hwang, J.P., González-Billalabeitia, E., Hung, M.C., et al. (2017). A UBE2O-AMPKα2 Axis that Promotes Tumor Initiation and Progression Offers Opportunities for Therapy. Cancer Cell *31*, 208–224. https://doi.org/10.1016/j.ccell.2017.01.003.

27. Huang, X., Tan, J., Ji, Y., Luo, J., Zhao, Y., and Zhao, J. (2024). BRCC3 mediates inflammation and pyroptosis in cerebral ischemia/reperfusion injury by activating the NLRP6 inflammasome. CNS Neurosci. Ther. *30*, e14697. https://doi.org/10.1111/cns.14697.

28. He, K., Wan, T., Wang, D., Hu, J., Zhou, T., Tao, W., Wei, Z., Lu, Q., Zhou, R., Tian, Z., et al. (2023). Gasdermin D licenses MHCII induction to maintain food tolerance in small intestine. Cell *186*, 3033–3048.e20. https://doi.org/10.1016/j.cell.2023.05.027.

29. Abramson, J., Adler, J., Dunger, J., Evans, R., Green, T., Pritzel, A., Ronneberger, O., Willmore, L., Ballard, A.J., Bambrick, J., et al. (2024). Accurate structure prediction of biomolecular interactions with AlphaFold 3. Nature *630*, 493–500. https://doi.org/10.1038/s41586-024-07487-w.

30. Xu, H., Yang, J., Gao, W., Li, L., Li, P., Zhang, L., Gong, Y.N., Peng, X., Xi, J.J., Chen, S., et al. (2014). Innate immune sensing of bacterial modifications of Rho GTPases by the Pyrin inflammasome. Nature *513*, 237–241. https://doi.org/10.1038/nature13449.

31. Dick, M.S., Sborgi, L., Rühl, S., Hiller, S., and Broz, P. (2016). ASC filament formation serves as a signal amplification mechanism for inflammasomes. Nat. Commun. *7*, 11929. https://doi.org/10.1038/ncomms11929.

32. Zhang, J., Yu, Q., Jiang, D., Yu, K., Yu, W., Chi, Z., Chen, S., Li, M., Yang, D., Wang, Z., et al. (2022). Epithelial Gasdermin D shapes the host-microbial interface by driving mucus layer formation. Sci. Immunol. *7*, eabk2092. https://doi.org/10.1126/sciimmunol.abk2092.

33. Zhu, H.H., Wu, D.P., Du, X., Zhang, X., Liu, L., Ma, J., Shao, Z.H., Ren, H.Y., Hu, J.D., Xu, K.L., et al. (2018). Oral arsenic plus retinoic acid versus intravenous arsenic plus retinoic acid for non-high-risk acute promyelocytic leukaemia: a non-inferiority, randomised phase 3 trial. Lancet Oncol. *19*, 871–879. https://doi.org/10.1016/s1470-2045(18)30295-x.

34. Dong, F., Chen, L., Zhao, C., Li, X., Tan, Y., Song, H., Jin, W., Zhu, H., Zhang, Y., Xue, K., et al. (2022). Predictive values of plasma TNFα and IL-8 for intracranial hemorrhage in patients with acute promyelocytic leukemia. Front. Med. *16*, 909–918. https://doi.org/10.1007/s11684-021-0890-1.

35. Fu, J., Schroder, K., and Wu, H. (2024). Mechanistic insights from inflammasome structures. Nat. Rev. Immunol. *24*, 518–535. https://doi.org/10.1038/s41577-024-00995-w.

36. Zheng, Q., Wang, T., Mao, J., Chu, G., Liang, L., Jing, Y., Zuo, C., Yu, Y., Hu, H., and Pan, M. (2023). A bifunctional molecule-assisted synthesis of mimics for use in probing the ubiquitination system. Nat. Protoc. *18*, 530–554. https://doi.org/10.1038/s41596-022-00761-z.

37. Satoshi. (2016). Trypsin Sensitivity Assay to Study the Folding Status of Proteins. Bio-Protoc. *6*, e1953.

38. Xu, C., Wang, S., Thibault, G., and Ng, D.T.W. (2013). Futile protein folding cycles in the ER are terminated by the unfolded protein O-mannosylation pathway. Science *340*, 978–981. https://doi.org/10.1126/science.1234055.

39. Izawa, T., Nagai, H., Endo, T., and Nishikawa, S. (2012). Yos9p and Hrd1p mediate ER retention of misfolded proteins for ER-associated degradation. Mol. Biol. Cell *23*, 1283–1293. https://doi.org/10.1091/mbc.E11-08-0722.

40. Song, B., Chen, Y., Liu, X., Yuan, F., Tan, E.Y.J., Lei, Y., Song, N., Han, Y., Pascal, B.D., Griffin, P.R., et al. (2021). Ordered assembly of the cytosolic RNA-sensing MDA5-MAVS signaling complex via binding to unanchored K63-linked poly-ubiquitin chains. Immunity *54*, 2218–2230.e5. https://doi.org/10.1016/j.immuni.2021.09.008.

41. Goswami, R., Gupta, A., Bednova, O., Coulombe, G., Patel, D., Rotello, V.M., and Leyton, J.V. (2024). Nuclear localization signal-tagged systems: relevant nuclear import principles in the context of current therapeutic design. Chem. Soc. Rev. *53*, 204–226. https://doi.org/10.1039/d1cs00269d.

42. Qu, Y., Misaghi, S., Izrael-Tomasevic, A., Newton, K., Gilmour, L.L., Lamkanfi, M., Louie, S., Kayagaki, N., Liu, J., Kömüves, L., et al. (2012). Phosphorylation of NLRC4 is critical for inflammasome activation. Nature *490*, 539–542. https://doi.org/10.1038/nature11429.

43. Andreeva, L., David, L., Rawson, S., Shen, C., Pasricha, T., Pelegrin, P., and Wu, H. (2021). NLRP3 cages revealed by full-length mouse NLRP3 structure control pathway activation. Cell *184*, 6299–6312.e22. https://doi.org/10.1016/j.cell.2021.11.011.

44. Hochheiser, I.V., Pilsl, M., Hagelueken, G., Moecking, J., Marleaux, M., Brinkschulte, R., Latz, E., Engel, C., and Geyer, M. (2022). Structure of the NLRP3 decamer bound to the cytokine release inhibitor CRID3. Nature *604*, 184–189. https://doi.org/10.1038/s41586-022-04467-w.

45. Liu, H., Zhang, H., Wu, X., Ma, D., Wu, J., Wang, L., Jiang, Y., Fei, Y., Zhu, C., Tan, R., et al. (2018). Nuclear cGAS suppresses DNA repair and promotes tumorigenesis. Nature *563*, 131–136. https://doi.org/10.1038/s41586-018-0629-6.

46. Coll, R.C., and Schroder, K. (2024). Inflammasome components as new therapeutic targets in inflammatory disease. Nat. Rev. Immunol. *25*, 22–41. https://doi.org/10.1038/s41577-024-01075-9.

47. Zhang, X.W., Yan, X.J., Zhou, Z.R., Yang, F.F., Wu, Z.Y., Sun, H.B., Liang, W.X., Song, A.X., Lallemand-Breitenbach, V., Jeanne, M., et al. (2010). Arsenic trioxide controls the fate of the PML-RARalpha oncoprotein by directly binding PML. Science *328*, 240–243. https://doi.org/10.1126/science.1183424.

48. Au, W.Y., Kumana, C.R., Kou, M., Mak, R., Chan, G.C.F., Lam, C.W., and Kwong, Y.L. (2003). Oral arsenic trioxide in the treatment of relapsed acute promyelocytic leukemia. Blood *102*, 407–408. https://doi.org/10.1182/blood-2003-01-0298.

49. Zhu, H.H., Hu, J., Lo-Coco, F., and Jin, J. (2019). The simpler, the better: oral arsenic for acute promyelocytic leukemia. Blood *134*, 597–605. https://doi.org/10.1182/blood.2019000760.

STAR★METHODS

KEY RESOURCES TABLE

REAGENT or RESOURCE	SOURCE	IDENTIFIER
Antibodies		
Goat polyclonal anti-murine NLRP6 antibody(E20)	Santa Cruz Biotechnology	Cat#: sc-50635; RRID: AB_2152563
Rabbit polyclonal anti- murine NLRP6 antibody	Sigma–Aldrich	Cat#: SAB1302240; RRID: AB_2750643
NLRP6 Polyclonal antibody	Proteintech	Cat# 30973-1-AP; RRID:AB_3669800
Mouse monoclonal anti-caspase-1 antibody	Adipogen	Cat#: AG-20B-0042; RRID: AB_2490248
Mouse monoclonal anti-FLAG antibody	Sigma–Aldrich	Cat#: F1804; RRID: AB_262044
Rabbit polyclonal anti-FLAG antibody	Proteintech	Cat#: 20543; RRID: AB_11232216
Rabbit monoclonal anti-HA antibody	Cell Signaling Technology	Cat#: 3724S; RRID: AB_1549585
Rabbit polyclonal anti-HA antibody	Proteintech	Cat#: 51064; RRID: AB_2935603
Rabbit polyclonal anti-GFP antibody	Proteintech	Cat# 50430-2-AP; RRID: AB_11042881
Mouse monoclonal anti-Myc antibody	Proteintech	Cat#: 60003-2-Ig; RRID: AB_2734122
Mouse monoclonal anti-Beta Actin antibody	Proteintech	Cat#: 66009-1-Ig; RRID: AB_2687938
Mouse monoclonal anti- GAPDH antibody	Proteintech	Cat#: 60004-1-Ig; RRID: AB_2107436
Mouse monoclonal anti- Lamin B1 antibody	Proteintech	Cat#: 66095-1-Ig; RRID: AB_11232208
Rabbit polyclonal anti-UBE2O antibody	Cell Signaling Technology	Cat#: 83393S; RRID: AB_2800015
Rabbit polyclonal anti-Ubiquitin antibody	Cell Signaling Technology	Cat#: 58395S; RRID: AB_3075532
Rabbit monoclonal anti-ASC antibody	Cell Signaling Technology	Cat# 67824; RRID: AB_2799736
Rabbit monoclonal anti-GSDMD antibody	Abcam	Cat# ab219800; RRID: AB_2888940
Goat anti-mouse IgG-HRP	Beyotime	Cat# A0216; RRID: AB_2860575
Goat anti-rabbit IgG-HRP	Beyotime	Cat# A0208; RRID: AB_2892644
FITC-conjugated goat anti-rabbit IgG	Invitrogen	Cat#: 65-6111; RRID: AB_2533966
Alexa Fluor 488-conjugated goat anti-mouse IgG	Servicebio	Cat#: GB25301; RRID: AB_2904018
Cy3-conjugated goat anti-rabbit IgG	Servicebio	Cat#: GB21303; RRID: AB_2861435
Bacterial and virus strains		
E. coli BL21(DE3)	New England Biolabs	Cat#: C2527
E. coli DH5α	New England Biolabs	Cat#: C2987
Citrobacter rodentium (ICC180)	ATCC	Cat#: 51459
Rotavirus (EC strain)	Harry Greenberg Lab	N/A
Listeria	ATCC	Cat#:15313
Biological samples		
Fetal Bovine Serum	Thermo Fisher Scientific	Cat#: 10091148
Chemicals, peptides, and recombinant proteins		
0.5M EDTA pH = 8.0	Biosharp	Cat#: BL581A
DMEM, High Glucose, Pyruvate	KeyGEN BioTECH	Cat#: KGL1211
4% paraformaldehyde	Servicebio	Cat#: G1101
DAPI	Biolegend	Cat#: 422801
Hoechst 33342	MedChemExpress	Cat#: HY-15559
Penicillin-streptomycin	Gibco	Cat#: 10378016
Immobilon Western Chemiluminescent HRP Substrate	Millipore	Cat#: WBKLS0500
Opti-MEM	Thermo Fisher Scientific	Cat#: 32985070
PBS	Servicebio	Cat#: G4202
Polybrene	Beyotime	Cat#: C0351
Puromycin	Beyotime	Cat#: ST551
PEI	Polysciences	Cat#: 23966-1
Lipofectamine 2000	Thermo Fisher Scientific	Cat#: 11668019

(*Continued on next page*)

Continued

REAGENT or RESOURCE	SOURCE	IDENTIFIER
BSA	Sigma-Aldrich	Cat#: A1933
Poly(I:C) HMW	Invivogen	tlrl-pic
Anti-Flag agrose beads	Sigma-Aldrich	Cat#: A2220
Anti-HA Magnetic Beads	MedChemExpress	Cat#: HY-K0201
NEM	Sangon Biotech	Cat#: A600450
IPTG	Sangon Biotech	Cat#: A100487
TEV protease	Sangon Biotech	Cat#: C500302
Coomassie brilliant blue R-250, 2X Solution	Sangon Biotech	Cat#: A602151
PMSF	Beyotime	Cat#:ST505
RIPA	Beyotime	Cat#: P0013B
NP-40	Beyotime	Cat#: P0013F
Nuclear and cytoplasmic protein extraction kit	Beyotime	Cat#: P0028
Glutathione beads	Smart Lifesciences	Cat#: SA008005
Ni IDA beads	Smart Lifesciences	Cat#: SA003005
Glutathione reduced	Sangon Biotech	Cat#: A600229
Imidazole	Sangon Biotech	Cat#: A600277
Ampicillin sodium	Sangon Biotech	Cat#: A610029
Neomycin trisulfate salt hydrate	Sangon Biotech	Cat#: A610366
Metronidazole	Sangon Biotech	Cat#: A600633
Vancomycin hydrochloride	Sangon Biotech	Cat#: A600983
Protease inhibitor cocktail	Roche	Cat#: 04693132001
Arsen oxide	Sigma-Aldrich	Cat#: A1010
Retinoic acid	MedChemExpress	Cat#: HY-14649
SYBR qPCR Master MIX	Vazyme	Cat#: Q311-02
HiScript® III RT SuperMix for qPCR	Vazyme	Cat#: R323-01
TRNzol Universal Reagent	TIANGEN	Cat#: 4992730
Advanced DMEM/F12	Gibco	Cat#: 12634-010
B27 supplement (50X)	Gibco	Cat#: 12587-010
Cell Recovery Solution	Corning	Cat#: 354253
Collagen from human placenta (type IV)	Sigma-Aldrich	Cat#: C5533
GlutaMAX (100X)	Gibco	Cat#: 35050-061
N2 supplement (100X)	Gibco	Cat#: 17502-048
rh-laminin-521	Gibco	Cat#: A29248
CD 293 01	Jianshun Biosciences	Cat#:11203-22052
CD 293 FC	Jianshun Biosciences	Cat#: 99151-23016
Erythrocytes lysate	Biosharp	Cat#: BL503A
Critical commercial assays		
Mouse IL-18 ELISA kit	Invitrogen	Cat#: BMS618
Human IL-18 ELISA kit	SinoBiological	Cat#: SEK10119
Experimental models: Cell lines		
HEK293T cells	ATCC	CRL-3216
293F cells	ATCC	CRL1573
HCT116 cells	ATCC	CCL-247
CT26 cells	ATCC	CRL-2638
HeLa cells	ATCC	CRM-CCL-2
Experimental models: Organisms/strains		
Nlrp6^{3xFlag} mice	Richard Flavell Lab	N/A
Nlrp6^{DKR} mutant mice	This paper	N/A
Villin-cre mice	Rongbin Zhou Lab	N/A

(*Continued on next page*)

Continued		
REAGENT or RESOURCE	SOURCE	IDENTIFIER
Nlrp6^{KO} mice	Richard Flavell Lab	N/A
UBE2O-floxed mice	GemPharmatech Co., Ltd	T005137
Oligonucleotides		
Primer set for plasmid constructions	TSINGKE	N/A
Quantitative real-time PCR Primers, see Table S3	TSINGKE	N/A
Recombinant DNA		
Plasmids, see Table S4	TSINGKE	N/A
Software and algorithms		
ImageJ	NIH	https://imagej.nih.gov/ij/
ZEN (black edition) v2.3	USTC	N/A
FlowJo software version 10.6.2	FlowJo, LLC	https://www.flowjo.com/
Prism version 8	Graphpad	https://www.graphpad.com/
Image Lab 6.1	Image Lab 5.2.1	
SnapGene 6.0.2	SnapGene	https://www.snapgene.com/
Bio-Rad CFX Manager 3.1	Bio-Rad CFX Manager	https://www.bio-rad.com/en-hk/sku/
SlideViewer 2.8	3DHISTECH	https://www.3dhistech.com/research/software-downloads/
HDX Workbench	Omics Informatics	http://hdxworkbench.com
Chimera	UCSF ChimeraX 1.8	https://www.cgl.ucsf.edu/chimera/download.html
Origin	OriginLab	https://www.originlab.com/
Other		
Immobilon®-P PVDF membrane	Millipore	IPVH00010
Millex-GP Filter, 0.22 μm	Millipore	SLGP033NS
35 mm glass bottom dish	Cellvis	D35-20-1.5-N
96 Well ELISA Plate	Nest	504201
HiLoad 16/600 superdex 200 pg	Sigma	GE28-9893-35

EXPERIMENTAL MODEL AND STUDY PARTICIPANT DETAILS

Human samples

All human samples used in the present study were obtained with the approval of the first affiliated hospital of the USTC (Anhui Provincial Hospital) (2025KY241). Informed consent was obtained from all patients for being included in the study. Blood sample from APL patients ($n = 6$) were collected from the Ruijin Hospital Affiliated to Shanghai Jiao Tong University School of Medicine (Shanghai, China) ($n = 3$), the First Affiliated Hospital of University of Science and Technology of China (Hefei, China) ($n = 2$), the Zhujiang Hospital of Southern Medical University (Guangzhou, China) ($n = 1$). Fecal sample from APL patients ($n = 5$) were collected from the Ruijin Hospital Affiliated to Shanghai Jiao Tong University School of Medicine (Shanghai, China) ($n = 3$), the First Affiliated Hospital of University of Science and Technology of China (Hefei, China) ($n = 1$), the Zhujiang Hospital of Southern Medical University (Guangzhou, China) ($n = 1$). More information is shown in the Table S1.

Mice

All mouse strains used in this paper are on C57BL/6 background. Two sgRNAs (CCCTTGTCACATCCTCTGAA-AGG and CCTTGTCACATCCTCTGAAA-GGG) that match reverse strand of *Nlrp6* and one ssDNA contains mutation of *Nlrp6* amino acids K115/116/117/128/130 (K115-130) to R115/116/117/128/130 (R115-130) and K680/682/683/684/685/686/687 (K680-687) to R680/682/683/684/685/686/687 (R680-687) were used to generate *Nlrp6*^{DKR} mutant strain by CRISPR–Cas9 technology. Genotyping of *Nlrp6*^{DKR} mice was performed using primers 5′-CTGGAGA AGGAAGCTATAGCATACTAG-3′ and 5′-AGAGCCGATTAA AAGTGTGCGTG-3′ with amplicons of a 328-bp product for sequencing, and using 5′-TTGGACTGGAG CTGCTGTACTGC-3′ and 5′-CTTCACCAGGCTCTTCTTCTT -3′ with amplicons of a 233-bp product for sequencing. UBE2O-floxed mice were purchased from GemPharmatech Co., Ltd. Villin-cre mice were provided by Dr. Rongbin Zhou. Genotyping of UBE2O-floxed mice was performed using primers 5′-TAGCAACCACTTACAGGTTGTCC-3′ and 5′-CTACCCTCTGACCTTGGCTCAT-3′ with amplicons of a 315-bp product from the wild-type allele and a 369-bp product from the targeted allele. In addition, the *UBE2O*$^{f/f}$ mice were crossed with Villin-cre transgenic mice that express Cre recombinase in villus and crypt epithelial cells of the small and large intestines to generate IECs-specific UBE2O-knockout mice. *Nlrp6*^{3xFlag} and *Nlrp6*^{KO} mice were provided by Dr. Richard Flavell and were

described in our previous report.[11] The co-housing littermate mice were used as the controls in most of the studies otherwise indicated. Mice were maintained under a 12-hour light-dark cycle at 23°C and approximately 50% humidity, and had free access to water and standard rodent diet under SPF condition. All animal experiments were approved by the Ethics Committee of University of Science and Technology of China (ethics code: USTCACUC24120124027).

Citrobacter rodentium infection model in mice

C. rod (ICC180) was obtained from ATCC (Manassas, VA, USA). *C. rod* infection model was performed as previously described.[4] Age- and gender-matched 6- to 8-week-old mice on the C57BL/6J (WT) background were used. Briefly, mice (WT, *Ube2o*$^{f/f}$, *Ube2o*$^{\Delta IEC}$, *Nlrp6*^{DKR}, *Ube2o*$^{f/f}$ *Nlrp6*^{KO}, *Ube2o*$^{\Delta IEC}$ *Nlrp6*^{KO}) were fasted overnight followed by challenging with *C. rod* via intragastric gavage. For inoculations, *C. rod* was prepared by shaking the bacteria in Luria-Bertani broth at 37 °C overnight. Mice were infected with 5×10^8 CFU of *C. rod* in a total volume of 200 μL per mouse by oral gavage. The fecal specimen was removed aseptically, weighed and homogenized in PBS on day 8 post infection. Then, the homogenates were serially diluted in PBS, plated on MacConkey agar plates and plates with nalidixic acid and kanamycin, then incubated overnight at 37°C. Bacterial colonies were enumerated and normalized to the fecal weight (per gram). On day 8 post intragastric administration, the mice were subjected to optical imaging *in vivo*, and IVIS Spectrum instrument (Caliper, PerkinElmer) was used to collect images and livingImages4.3.1 software for data analysis.

Rotavirus infection model in mice

Rotavirus infection model was performed as we previously described.[7,9] Briefly, stock virus (EC strain) was prepared by infecting 5-day-old C57BL/6J mice, and harvesting crude centrifugation-clarified intestinal homogenate. Then, 6-week-old mice (WT, *Ube2o*$^{f/f}$, *Ube2o*$^{\Delta IEC}$, *Nlrp6*^{DKR}, *Ube2o*$^{f/f}$ *Nlrp6*^{KO}, *Ube2o*$^{\Delta IEC}$ *Nlrp6*^{KO}) were orally inoculated by gavage with 50% diarrhea dose (DD50) of EC virus in 200 μL sterile PBS for the infection with EC strain for 3 days. Mice were sacrificed, and small intestinal tissues and mLNs were collected at indicated time points. Viral loads and ISG expression in tissues were detected by quantitative real-time PCR.

Cell lines, transfection, and cell sorting

All plasmids used in this study are included in Table S4. HEK293T cells (CRL-3216), HeLa cells (CCL-2), HCT116 cells (CCL-247), and CT26 (CRL-2638) cells were maintained in Dulbecco's Modified Eagle Medium (DMEM, Life Technologies) containing antibiotics (Life Technologies) and 10% fetal bovine serum (Life Technologies). These cell lines are not listed in the database of commonly misidentified cell lines maintained by ICLAC, and were tested to eliminate the possibility of mycoplasma contamination. For transient transfection, NLRP6 (NM_133946.2), ASC (NM_023258.4), GSDMD (NM_026960), Caspase-1 (NM_009807.2), UBE2O (NM_173755.4), KPNA1 (NM_001416718.1), KPNA2 (NM_010655.3), KPNA4 (NM_008467.4), KPNA6 (NM_008468.4) and other indicated genes were cloned into the pcDNA vector and transfected using PEI (Polysciences, 23966-1) or Lipofectamine 2000 (ThermoFisher, 11668019). For stable transfection, the genes encoding NLRP6, NLRP6 mutants, ASC, UBE2O, UBE2O C1037S were inserted into the pLVX vector. The plasmids were co-transfected with pMD2.g and pSPAX2 viral packaging plasmids using PEI. 6 hours after transfection, cells were cultured with DMEM containing 20% FBS for an additional 36 h. The culture medium containing lentivirus particles was filtered through a 0.45-μm PVDF filter (Millipore) and incubated with HEK293T, HeLa, HCT116 and CT26 cells supplemented with 8 μg/mL polybrene (Sigma-Aldrich) for 24 h followed by selection with 2 μg/ml puromycin (Beyotime) for another 24 h. Finally, the cells were expanded further in normal media, either for subsequent imaging or Western blotting. For sorting of GFP-positive or/and mCherry-positive cells, cells were FACS-sorted (FACSAria Fusion or FACSAria III, BD) based on GFP and mCherry expression level using 488-nm and 561-nm laser. All samples from FACS-sorted cells were treated with Hoechst (Beyotime) and imaged using a LSM880 laser scanning microscope with 20× and 63× objective. For all transfection assay, the plasmids were co-transfected using Lipofectamine 2000, lipofectamine 3000 or PEI. Six hours after transfection, cells were cultured with DMEM containing 20% FBS for an additional 48 h. Please refer to key resources table and Table S4 for the plasmids list.

Isolation of IECs and IELs in the intestine

Small intestines were excised and flushed thoroughly three times with PBS. They were turned inside out and cut into ~1 cm sections then transferred into RPMI with 2 mM EDTA, and shaken for 20 min at 37°C. Supernatants were collected through a 100-mesh cell strainer to get single-cell suspensions. Cells were collected as the IEC fraction which contains both epithelial cells (~90%) and lymphocytes (IEL, ~10%). Single-cell suspension was used for further analysis.

METHOD DETAILS

Protein expression

The DNA sequence encoding NLRP6 and mutants were cloned into pGEX-6p-1 vector and UBE2O was cloned into pET-28a-His vector. The constructs were transformed into E. coli Rosetta 2 (DE3) and induced with IPTG for 16 h at 16°C after the cells were cultured at 37°C until the OD600 nm reached 0.6. GST-fusion proteins were purified by glutathione affinity chromatography. His-tagged proteins were purified by immobilized metal ion affinity chromatography. For 293F cell expression system, the DNA sequence encoding NLRP6 was cloned into PTT5 vector. The 293F cell was cultured with CD 293 01 medium at 37°C, 5% CO_2, and shaked at 110 rpm till

the cell count achieved 2*10^6/mL. The 293F cell was transfected with the indicated plasmids, and CD 293 FC was added 24 h later. The cells were harvested after 2 days.

GST-tag protein purification with FPLC from *E. coli* BL21

The E.coli BL21 expressing target protein was resuspended in pull-down buffer (50 mM Tris-HCl, 200 mM NaCl, 1 mM EDTA, 10 mM $MgCl_2$, 1 mM DTT, 1% NP-40, pH = 8.0) supplemented with PMSF and lyzosome, and lysed by ultrasonic (30 min, 40% power, 4 s on, 3 s off). The lysate was centrifuged at 12000 rpm for 10 min. The supernatant was collected and filtered with 0.45 μm strainer, and rotate with GST-tag Purification Resin (beyotime) for 1 h at 4°C. The mix was then put into the affinity chromatography column, and washed with pull-down buffer for 2 times and wash buffer (50 mM Tris-HCl, 500 mM NaCl, 1 mM EDTA, 10 mM $MgCl_2$, 1 mM DTT, 1% NP-40, pH = 8.0) for 2 times. The purified protein was eluted with elution buffer (50 mM Tris-HCl, 10 mM GSH, pH = 8.0) and concentrated by ultrafiltration, and separated by molecular weight with FPLC. Briefly, protein purification was performed by size-exclusion chromatography (SEC) using an ÄKTA go FPLC system (Cytiva) equipped with a HiLoad 16/600 Superdex 200 pg prep-grade column (Cytiva). The column was equilibrated with 120 mL of binding buffer at a constant flow rate of 1 mL/min. Clarified protein sample, obtained by centrifugation at 12,000 rpm for 30 minutes, was loaded onto the column via the system's sample injector. Elution was monitored by continuous UV absorbance at 280 nm. Fractions corresponding to the UV peak elution profile characteristic of the target protein were collected. These fractions were subsequently analyzed by SDS-PAGE to confirm the presence and purity of the desired protein. Positive fractions containing the target protein were pooled and concentrated to the desired final concentration, and archived at -80°C until further use.

His-tag protein purification with FPLC from 293F

The 293F cell was resuspended with Lysis Buffer (50 mM NaH_2PO_4, 300 mM NaCl, 10 mM imidazole, pH = 8.0) supplemented with PMSF, and lysed by ultrasonic (30 min, 40% power, 4 s on, 3 s off). The lysate was centrifuged at 12000 rpm for 10min. The supernatant was collected and filtered with 0.45 μm strainer, and added into the Ni-NTA Beads 6FF column (Smart-Lifesciences) which was pre-balanced with Lysis Buffer. The column was washed with Wash Buffer (50 mM NaH_2PO_4, 300 mM NaCl, 20 mM imidazole, pH = 8.0). The purified protein was eluted with Elution Buffer (50 mM NaH_2PO_4, 300 mM NaCl, 250 mM imidazole, pH = 8.0) and concentrated by ultrafiltration, and separated by molecular weight with FPLC. Briefly, protein purification was performed by size-exclusion chromatography (SEC) using an ÄKTA go FPLC system (Cytiva) equipped with a HiLoad 16/600 Superdex 200 pg prep-grade column (Cytiva). The column was equilibrated with 120 mL of binding buffer at a constant flow rate of 1 mL/min. Clarified protein sample, obtained by centrifugation at 12,000 rpm for 30 minutes, was loaded onto the column via the system's sample injector. Elution was monitored by continuous UV absorbance at 280 nm. Fractions corresponding to the UV peak elution profile characteristic of the target protein were collected. These fractions were subsequently analyzed by SDS-PAGE to confirm the presence and purity of the desired protein. Positive fractions containing the target protein were pooled and concentrated to the desired final concentration, and archived at -80°C until further use.

GST pull-down, immunoprecipitation, and immunoblotting

GST pull-down and immunoprecipitation were performed as we previously described.[28] Briefly, for the GST pull-down assay, GST-fusion proteins immobilized on glutathione beads were incubated with the indicated proteins in the pull-down buffer (50 mM Tris-HCl, pH 7.4, 150 mM NaCl, and 0.5% Triton X-100) for 4 h at 4°C after purification of GST-fusion proteins and tag-free proteins. Beads were washed five times with pull-down buffer and the bound proteins were eluted by boiling in loading buffer. Input and bead-bound proteins were analyzed by Western blot. For the immunoprecipitation assay, HEK293T cells transfected with indicated plasmids, intestinal tissues or IECs were harvested and resuspended in 1 mL ice-cold Pierce IP buffer (50 mM Tris-HCl, pH 7.4, 1.0% NP-40, 0.5% Triton X-100, 150 mM NaCl, 1.0 mM MgCl2, 1.0 mM EDTA, and 15% glycerol) supplemented with PMSF and phosphatase inhibitor NaF and NaVO3. Cell lysates were pre-cleared with protein A/G-coupled Sepharose beads for 2 h before they were immunoprecipitated with the indicated antibodies. Then, the samples were analyzed by SDS-PAGE, and transferred to PVDF membranes (Millipore). Membranes were detected with specific primary antibodies and secondary horseradish peroxidase-conjugated anti-mouse or rabbit antibodies. Immunoreactive bands were visualized using the enhanced chemiluminescence reagent (Nature biosciences). NEM must be added to lysates of all cells and tissues for detection of monoubiquitination. For *in vivo* experiments, intestinal tissues were sampled after oral administration with AsIII for 3 days. For experiments in cells, cells were treated with 1 μM AsIII for 24 h. 0.4 mg per mice is a clinically relevant dose for oral administration.

HDX-MS

We purified $NLRP6^{1\text{-}687}$, $NLRP6^{1\text{-}687}$-Ub^{CT}, $NLRP6^{115\text{-}869}$ and Ub^{NT}-$NLRP6^{115\text{-}869}$ with FPLC from *E. coli* BL21, and then HDX-MS was carried out by Zheng Jie Lab as previously described.[40] Briefly, before the reaction, 5 μM purified target protein were incubated on ice with 50 μM GRL-0617 or SIMM-036 in buffer (50 mM HEPES, pH 7.5, 50 mM NaCl, 4 mM $MgCl_2$, 2 mM DTT) for 30 min. Four-microliter of protein/protein complex with ligand/peptide was diluted into 16 μL D_2O on exchange buffer (50 mM HEPES, pH 7.5, 50 mM NaCl), and incubated for certain time points at 4°C. The samples were quenched by mixing with 20 μL 1% trifluoroacetic acid, and was immediately injected into the LEAP Pal 3.0 HDX platform. Samples went through an immobilized pepsin column (2 mm × 2 cm) at 120 μL min^{-1}, and the digested peptides were trapped by a C18 PepMap300 trap column (Thermo Fisher Scientific) and desalted at 4°C. The digested peptides were separated across a 2.1 mm × 5 cm C18 separating column (1.9 μm Hypersil Gold,

Thermo Fisher Scientific) with a linear gradient of 4%–40% CH_3CN and 0.3% formic acid, over 6 min, at 4°C. Mass spectrometric data were acquired using a Fusion Orbitrap mass spectrometer (Thermo Fisher Scientific) with a measured resolving power of 65000 at m/z 400. HDX analyses were performed in triplicate, with single preparations of each protein ligand complex. The intensity weighted mean m/z centroid value of each peptide envelope was calculated and subsequently converted into a percentage of deuterium incorporation. Statistical significance for the differential HDX data is determined by an unpaired t-test for each time point, a procedure that is integrated into the HDX Workbench software. Corrections for back-exchange were made on the basis of an estimated 70% deuterium recovery, and accounting for the known 80% deuterium content of the deuterium exchange buffer.

Trypsin sensitivity assay

Trypsin sensitivity assay was carried out as previously described.[38] Briefly, cells transfected with target plasmids were harvested and lysed with lysis buffer, and digested by trypsin (50 μg/mL) at 4 °C for 5 min. The reaction was ended by adding 3×loading buffer and boiling at 100 °C for 10 min. The level of target protein remain was measured by Western-blotting. Relative target protein level was measured by quantitative immunoblotting and protein level of actin served as a control for normalization.

Optimized ASC-NLRs immunoprecipitation

Because NLRs aggregate dramatically with ASC in the pellet upon transfected into HEK293T cells,[4,6,8] it is difficult to detect NLRs-ASC interaction in the supernatant with conventional IP buffer and we thus optimized immunoprecipitation assay. Briefly, HEK293T cells were transfected with indicated plasmids and HA-ASC, and cultured for 24 h. Then cells were harvested and resuspended in 100 μL ice-cold RIPA buffer (50 mM Tris-HCl, pH 7.4, 0.1% SDS, 1.0% sodium deoxycholate, 1.0% Triton X-100, 150 mM NaCl, 1.0 mM $MgCl_2$, 1.0 mM EDTA) supplemented with PMSF and phosphatase inhibitor NaF and NaVO3 for 0.5 h. Then 900 μL of NP-40 buffer (50 mM Tris-HCl, pH 7.4, 150 mM NaCl, 1.0 mM MgCl2, 1.0 mM EDTA) was added to the sample and make a tenfold dilution of the SDS to 0.01%. Samples were further incubated on ice for 0.5 h and centrifuged at 6000 rpm for 5 minutes at 4°C, followed by conventional IP analysis.

IP-LC-MS/MS

LC-MS/MS based on pulldown analysis was performed as we previously described.[28] To identify NLRP6-interacting proteins, we employed a GST pull-down experiment. Briefly, GST-NLRP6 and GST control were expressed in BL21 (DE3), and purified with Glutathione Beads. These purified proteins were then incubated with IEC cell lysates for 2 hours at 4°C. After extensive washing, bead-bound proteins were separated by SDS-PAGE and visualized by Coomassie blue staining. The strong protein bands specifically present in GST-NLRP6 pull-down complex were analyzed by mass spectrometry (APTbiotech, Shanghai CN), and a ~220 kDa protein band was identified as UBE2O. For the identification of NLRP6 modification types in vivo, IECs from Nlrp63xFlag mice were harvested and resuspended in 1 mL ice-cold Pierce IP buffer (50 mM Tris-HCl, pH 7.4, 1.0% NP-40, 0.5% Triton X-100, 150 mM NaCl, 1.0 mM $MgCl_2$, 1.0 mM EDTA, and 15% glycerol) supplemented with PMSF and phosphatase inhibitor NaF and $NaVO_3$. Cell lysates were immunoprecipitated with the anti-Flag antibodies. Then, the samples were analyzed by mass spectrometry (APTbiotech, Shanghai CN).

Ubiquitination assay

HEK293T cells were transfected with the indicated plasmids for twenty-four hours. Then, cells were treated with 20 μM MG132 for an additional 4 h. The in vivo ubiquitination assay was then performed according to the procedure described previously.[40] Briefly, cells were lysed in RIPA buffer (50 mM Tris-HCl, pH 7.5, 150 mM NaCl, 1 mM EDTA, 0.5% Triton X-100, 0.5% NP-40, 1% sodium deoxycholates, 0.1% SDS, and 10 μM MG132, 5 mM NEM) supplemented with PMSF and phosphatase inhibitor NaF and $NaVO_3$. Cell lysates were incubated with anti-Flag M2 affinity beads at 4°C for 4 h. The immunoprecipitates and input were then subjected to Western blot analysis to detect NLRP6 ubiquitination. Alternatively, cells were lysed in denaturing buffer (6 M guanidine-HCl, 0.1 M $Na2HPO_4$/$NaH2PO_4$, 10 mM imidazole, pH 8.0). Cell lysates were incubated with Ni-NTA agarose beads to pull down proteins conjugated to HA-ubiquitin. Beads-bound proteins were then analyzed by Western blotting with anti-NLRP6, anti-Flag, anti-UBE2O, anti-HA, and anti-Ub antibodies.

RNA interference

RNA interference was performed as previously described.[28] To generate lentiviruses expressing the indicated shRNAs, HEK293T cells grown on a 6-cm dish were transfected with 2 μg of shRNA cloned in PLKO.1 (Sigma-Aldrich, SHC001,) or control vector, 2 μg of pREV, 2 μg of pGag, and 1 μg of pVSVG. Six hours after transfection, cells were cultured with DMEM containing 20% FBS for an additional 48 h. The culture medium containing lentivirus particles was filtered through a 0.45-μm PVDF filter (Millipore) and incubated with HEK293T, HeLa or BMDMs cells supplemented with 8 μg/mL polybrene (Sigma-Aldrich) for 24 h followed by selection with 2 μg/ml puromycin for another 24 h. Then, cells were harvested and analyzed by Western blotting. The shRNA target sequences used in this study are as follows: sh-control (CCTAAGGTTAAGTCGCCCTCG); sh-hUBE2O-#1 (CCAGAGGTTTACAAGTTTC); sh-hUBE2O-#2 (CCAACCCGAGAGAAGAAGTTT); sh-mUBE2O-#1 (CTACAACGAGATGGCATTAAT).

ELISA

For mouse IL-18, 0.5 cm-long colon pieces from the proximal colon were removed, rinsed with PBS, and weighed. The tissue explants were cultured for 6 h in DMEM medium containing 10% FBS, L-glutamine, penicillin, and streptomycin at 37°C. Culture medium was collected, centrifuged and the supernatants were stored in aliquots at -20°C or assayed for mouse IL-18 (Invitrogen, BMS618) according to the manufacturer's instructions. For human IL-18, fecal supernatants were obtained by homogenization in PBS (100 mg feces/mL) followed by centrifugation (8000 × g, 20 min, 4°C). Serum and fecal IL-18 levels were determined using human IL-18 kits (SinoBiological, Cat#: SEK10119) with 5-fold diluted samples according to the manufacturer's instructions.

Inflammasome reconstruction system in cells

Due to the predominantly expressed NLRP6 in IECs, and the high mortality and non-culturable as well as unpassaging of isolated IECs, we are limited to *in vivo* studies (e.g., assays form mouse model) of NLRP6 inflammasome activation while only ASC-NLRP6 immunoprecipitation assays can be performed to investigate the molecular mechanism.[4,6,8] Here, we reconstructed the NLRP6 inflammasome system in HEK293T cells. Briefly, HEK293T cells grown on a 6-cm dish were transfected with NLRP6, ASC, Casp1, and GSDMD for 24 h. Then, cells were harvested and resuspended in 100 μL ice-cold PBS containing 0.5% Triton X-100 for 15 min followed by centrifugation at 6800 g for 5 min. Triton X-100-soluble supernatants were boiled in Laemmli buffer for 5 min, and resolved by immunoblot analysis.

ASC oligomerization assay

ASC oligomerization assay was performed as previously described in macrophages.[18] We performed the ASC oligomerization analysis in the inflammasome reconstruction system within HEK293T cells. Briefly, HEK293T cells grown on a 6-cm dish were transfected with indicated plasmids for 24 h. Then, cells were harvested and resuspended in 100 μL ice-cold PBS containing 0.5% Triton X-100 for 15 min followed by centrifugation at 6800 g for 5 min. Triton X-100-soluble supernatants were detected as input. Triton X-100-insoluble pellets were washed three times with PBS, suspended in 200 μL PBS and then cross-linked at 25°C for 30 min by adding disuccinimidyl suberate (ThermoFisher, 21655). Reactions were terminated by adding Tris (20 mM) for 15 min at 25°C. The cross-linked pellets were centrifuged at 8000g for 15 min, boiled in Laemmli buffer for 5 min, and resolved by immunoblot analysis.

ASC filaments

ASC filaments assay was performed as previously described in macrophages. Briefly, HEK293T or HeLa cells were stably transfected with mouse ASC-mCherry and mouse NLRP6-GFP or its mutants for 24 h. Then, cells were treated with Hoechst and imaged using a LSM880 laser scanning microscope with 20× and 63× objective. For quantification, 5 randomly selected fields of one biological sample at 20× magnification were averaged to obtain a number of cells containing ASC filaments and 3 biological replicates were used to compare the differences.

LDH release assay

LDH release assay was performed as we previously described in iBMDM.[7] Briefly, HEK293T cells that were stably transfected with mouse ASC, Casp1, and GSDMD were subsequently transfected with NLRP6 or its mutant for 24 h. Test compounds and vehicle-only controls were added to the appropriate wells. Then treated assay plates were returned to the cell culture incubator for the duration of the treatment. After collecting and diluting all samples, 50 μL of diluted sample was transferred into a 96-well opaque-walled and added 50 μL of LDH detection reagent followed by incubation for 1 h at 25°C. Finally, the absorbance at 490 nm was recorded. Percent cytotoxicity = 100 × (experimental LDH release-medium background) / (maximum LDH release control-medium background).

SDD-AGE assay

HEK293T cells were transfected with indicated plasmids or its mutant for 36 h. Then, cells were harvested and resuspended with Triton X-100 lysis buffer and then re-suspended in 1× sample buffer and loaded onto a vertical 1.5% agarose gel with 1% SDS. After electrophoresis in running buffer (0.5 × TBE and 0.1% SDS) for 1 h at a constant voltage of 80 V at 4 °C, the proteins were transferred to PVDF membranes (Millipore) for immunoblotting. The buffers used were as follows: 1× TBE buffer: 90 mM Tris, pH 8.3, 90 mM boric acid, 2 mM EDTA; Triton X-100 lysis buffer: 0.5% Triton X-100, 50 mM Tris–HCl, 150 mM NaCl, 10% glycerol, 1 mM PMSF, and protease inhibitor cocktail; 1× sample buffer: 0.5×TBE, 10% glycerol, 2% SDS, and 0.0025% bromophenol blue.

Nuclear and cytoplasmic isolation assay

HEK293T cells or IECs were harvested and subjected to nuclear and cytoplasmic protein extraction by Nuclear and Cytoplasmic Protein Extraction Kit (Beyotime, P0027). The follow-up steps were carried out according to manufacturer's instructions. For the cytoplasmic extract, HeLa cells and IECs were lysed in buffer A and buffer B. Nuclei were then resuspended nuclear extraction buffer. Each fraction was quantified and proceeded to immunoblotting assay with the following primary antibodies: Anti-LAMB1, anti-GAPDH, anti-NLRP6 and anti-UBE2O.

RNA isolation, quantitative real-time PCR, and primers

All Primers used in this study are included in Table S4. Total RNAs were isolated from different cell lines, mouse tissues or IECs using TRIzol reagent (Invitrogen). The cDNA was synthesized from 500 ng of total RNA using the HiScript III RT SuperMix kit (Vazyme, CN) according to the manufacturer's instructions. After reverse transcription, quantitative real-time PCR was performed on the Bio-Rad CFX384 real-time PCR system in a 10 μL reaction system using SYBR Green qPCR Master Mix (Vazyme, CN). Gapdh, Actin or Hprt was used as an endogenous control. The mRNA expression levels of the tested genes relative to endogenous control were determined using the $2^{-\Delta\Delta Ct}$ method and shown as fold induction.

Immunofluorescence and live-cell imaging by confocal microscopy

For immunofluorescence assay, HeLa or HEK293T cells transduced with indicated plasmids were grown on cover slips in 24-well plates. After the corresponding experimental treatment, cells were fixed in 4% paraformaldehyde (PFA) for 30 min at room temperature and subsequently permeabilized and blocked with PBS containing 0.5% Triton-X-100 and 5% bovine serum albumin for 1 h at room temperature. samples were incubated with antibodies against the indicated proteins for 2 h at room temperature or 4°C overnight, followed by incubation with secondary antibody for 1 h. Nuclei were visualized with 40,6-diamidino-2-phenylindole (DAPI, Invitrogen). Mouse intestinal samples were fixed with 4% PFA and embedded in paraffin. NLRP6 staining was done in Xinle (Hefei, CN). For mucus layer staining, the 3 mm of the terminal colon containing feces was fixed in Carnoy's buffer for 24 hours and washed in absolute ethyl alcohol. Mucus staining was done in Ketu (Hefei, CN). The antibodies used for immunostaining were against NLRP6 antibody (Sigma-Aldrich, sab1302240) and MUC2 (Servicebio, GB11344). The secondary antibodies were FITC-conjugated goat anti-rabbit, FITC-conjugated goat anti-mouse, and Cy3-conjugated goat anti-rabbit. All fluorescence images were analyzed via confocal imaging using Zeiss LSM880. Nuclei were visualized with DAPI. For live-cell imaging, cells transfected with indicated lentivirus were FACS-sorted (FACSAria Fusion or FACSAria III, BD) based on GFP and mCherry expression level using 488-nm and 561-nm laser. FACS-sorted cells were further cultured for at least 3 generations and then imaged using a Zeiss LSM880 laser scanning microscope with 20 × and 63 × objective. Nuclei were visualized with Hoechst.

QUANTIFICATION AND STATISTICAL ANALYSIS

All data are presented as means ± SEM. Comparisons between groups were analyzed by unpaired two-tailed Student's t test, one-way analysis of variance (ANOVA) or two-way ANOVA. Statistical analysis was performed using GraphPad Prism 8. $P < 0.05$ was considered statistically significant (*$P < 0.05$, **$P < 0.01$, ***$P < 0.001$, and ****$P < 0.0001$; ns, not statistically significant). The sample sizes (biological replicates), specific statistical tests used, and the main effects of our statistical analyses for each experiment were detailed in each figure legend. Graphical abstract was generated using BioRender.